






**Contact effects on electron transport along disordered borophene nanoribbons with line defects**Pei-Jia Hu <sup>1,\*</sup>, Zeng-Ren Liang <sup>1,\*</sup>, Jia-Wen Sun <sup>1</sup>, Tie-Feng Fang <sup>2</sup>, Ai-Min Guo <sup>1,†</sup> and Qing-Feng Sun <sup>3,4</sup><sup>1</sup>*Human Key Laboratory for Super-microstructure and Ultrafast Process, School of Physics, Central South University, Changsha 410083, China*<sup>2</sup>*School of Sciences, Nantong University, Nantong 226019, China*<sup>3</sup>*International Center for Quantum Materials, School of Physics, Peking University, Beijing 100871, China*<sup>4</sup>*Hefei National Laboratory, Hefei 230088, China*

(Received 9 December 2023; revised 16 March 2024; accepted 10 April 2024; published 25 April 2024)

Line defects (LDs) in borophenes, which occur at the interface between two different boron sheets, have garnered considerable interest. Motivated by recent advancements in the synthesis of diverse borophene polymorphs and heterojunctions, we investigate the contact effects on electron transport through two-terminal disordered borophene nanoribbons (BNRs) with a random distribution of LDs. The source and drain are chosen from the following four semi-infinite electrodes:  $\nu_{1/5}$  BNR,  $\nu_{1/6}$  BNR,  $\nu_{1/3}$  BNR, and square lattice (SL). Despite the substantial reduction in the overall conductance of disordered BNRs, several resonant peaks can appear in the transmission spectra, regardless of inhomogeneous model parameters, nanoribbon length and width, and contact configuration. The amplitude of all the resonant peaks is exactly the conductance quantum  $G_0$  when both electrodes are taken as the  $\nu_{1/5}$  or  $\nu_{1/6}$  BNR. In contrast, the peak amplitude will be less than  $G_0$  when either electrode is taken as the  $\nu_{1/3}$  BNR or SL. Notably, some resonant peaks completely vanish for the contact configuration of the  $\nu_{1/3}$  BNR, a phenomenon termed as the resonant peak filtering effect, which can be understood from the structure-property relationships associated with the local current distribution. Additionally, the distribution of conductance at off-resonant energies can be well fitted by the Anderson localization theory. And the evolution of the resonant peaks with the nanoribbon width is also revealed. These findings contribute to the understanding of structure-property relationships, which is valuable for designing borophene-based nanodevices.

DOI: [10.1103/PhysRevB.109.165437](https://doi.org/10.1103/PhysRevB.109.165437)**I. INTRODUCTION**

Following the successful synthesis of graphene in 2004 [1], research on two-dimensional (2D) materials has entered a new era [2,3]. Owing to their unique electronic properties, such as high carrier mobility [4,5] and quantum confinement effects [6–8], 2D materials offer distinct advantages over three-dimensional counterparts. Over the past two decades, numerous 2D materials have been successfully synthesized, including silicene [9,10], germanene [11,12], black phosphorene [13], and borophene [14,15]. With the development of nanotechnology [16–19], these 2D materials find broad applications in the realm of nanoscale field-effect transistors [20–22], quantum computation [23], optoelectronics [24], and thermoelectric nanodevices [25].

The geometric structures of 2D materials is a crucial determinant that significantly impacts their physical properties. Borophene, in particular, stands out among numerous 2D materials due to its structural polymorphism arising from electron deficiency of boron [26–33]. It has been predicted that a variety of stable borophene phases could be prepared on different metal substrates by employing the cluster expansion

method for extrapolating boron clusters into 2D configuration [34,35], indicating that the borophene structures are sensitive to metal substrates. Since its initial experimental synthesis by two independent research groups [14,15], many borophene polymorphs have been successfully achieved [36–43], providing an excellent platform for enhancing our understanding of the structural-property relationships. These various borophene phases can be characterized as triangular lattices comprising boron atoms with unique patterns created by hollow hexagon vacancies [44], and various borophene phases are typically named according to their vacancy concentration,  $\nu$  [26]. For example, the  $\beta_{12}$ ,  $\chi_3$ , and honeycomb borophene sheets are named as  $\nu_{1/6}$ ,  $\nu_{1/5}$ , and  $\nu_{1/3}$ , respectively [15,39]. In addition, borophene nanoribbons (BNRs) with lengths extending to hundreds of nanometers have recently been synthesized [45,46], suggesting that the  $\nu_{1/6}$  and  $\nu_{1/5}$  BNRs can be viewed as composed of (2, 2) and (2, 3) boron chains, respectively. Here, the indices “ $a_n$ ” and “ $a_w$ ” in  $(a_n, a_w)$  represent the number of atoms in the narrow and wide rows of a single boron chain, respectively.

The electronic properties of borophene polymorphs have undergone extensive study, resulting in numerous remarkable advancements [47–55]. For instance, by employing high-resolution angle-resolved photoemission combined with first-principles calculations, Feng *et al.* substantiated the existence of Dirac fermions in  $\nu_{1/6}$  borophene [47]. Subsequently,

\*These authors contributed equally to this work.

†aimin.guo@csu.edu.cn

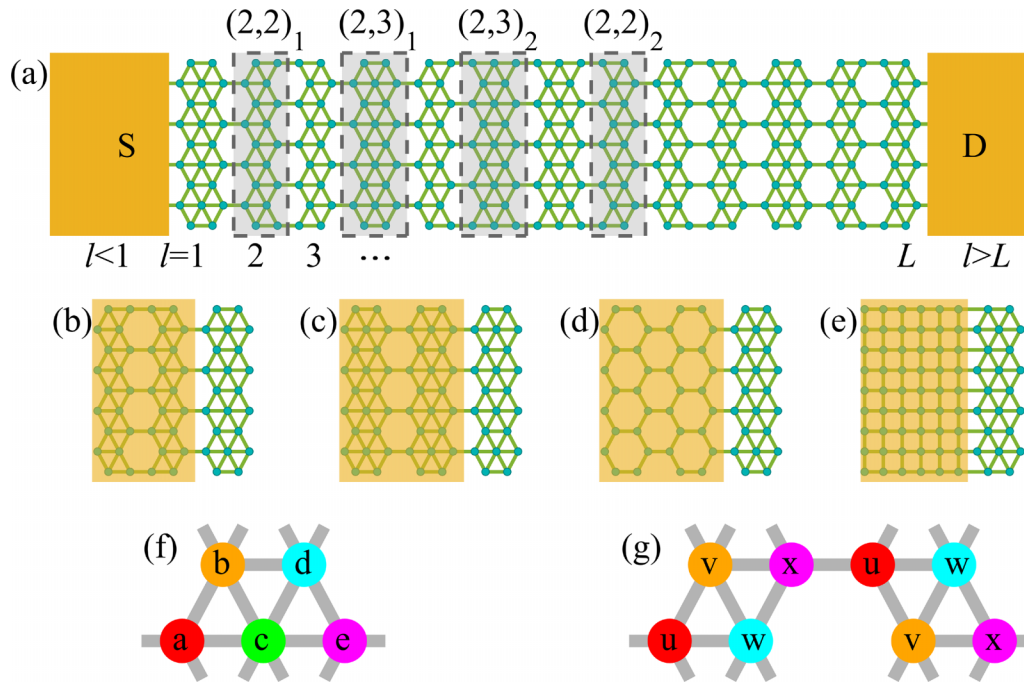


FIG. 1. (a) The schematic diagram depicts a two-terminal disordered BNR coupled to the source and drain at the left and right sides, represented as yellow rectangles. The CSR represents a disordered BNR with LDs assembled from a random arrangement of  $(2, 2)$  and  $(2, 3)$  chains. In this arrangement, a  $(2, 2)_j$  chain is randomly followed by either a  $(2, 2)_j$  or  $(2, 3)_j$  chain, and a  $(2, 3)_j$  chain is randomly followed by either a  $(2, 2)_j$  or  $(2, 3)_j$  chain. Here,  $\bar{j}$  is equal to 1 (2) when  $j$  is equal to 2 (1). The length of disordered BNR in (a) is  $L = 13$ , representing the number of chains in the CSR, and the width, defined as the number of rows, is  $N = 9$ . For different contact configurations, the source and drain can be selected from four semi-infinite electrodes: (b)  $\nu_{1/5}$  BNR, (c)  $\nu_{1/6}$  BNR, (d)  $\nu_{1/3}$  BNR, and (e) SL. (f) The unit cell of  $\nu_{1/6}$  borophene, which contains five boron atoms called as a, b, c, d, and e. (g) The unit cell of  $\nu_{1/5}$  one, which includes eight atoms labeled by u, v, w, and x.

other intriguing band properties, including triplet fermions [51] and a Dirac nodal line [52], are further theoretically demonstrated in the  $\nu_{1/6}$  borophene, suggesting the potential of monolayer boron for application in high-speed electron transport devices. Particularly, Norouzi *et al.* studied the charge and spin transport properties of the  $\nu_{1/6}$  BNR under the influence of an exchange magnetic field, finding that the  $\nu_{1/6}$  BNR could serve as an efficient spin filter [54]. Recently, several mixed-phase borophenes [56–62] and BNRs [46] with an intriguing line defect (LD) occurring at the interface between two different single phase borophenes, such as  $\nu_{1/6}$  and  $\nu_{1/5}$ , are widely observed in various experiments. Theoretical investigations further suggest that the  $(2, 2)$  and  $(2, 3)$  chains can serve as fundamental building blocks for constructing novel borophene phases with LDs [63] and reveal a series of exciting results, such as resonant tunneling [64], self-similarity [65], and negative differential resistance [66].

The phase intermixing of borophene naturally leads to the formation of borophene heterojunctions. New physical phenomena may arise by combining two or more 2D materials with different properties into 2D heterostructures [67–70]. Recently, several borophene heterostructures have been experimentally synthesized [71–74], providing a promising opportunity to explore the rich electron transport properties of borophenes by considering the contact effects. The contact effects play a crucial role in significantly influencing the electron transport properties of 2D materials

[75–88]. For example, Stegmann *et al.* studied the electron transport in graphene nanoribbons using microwave emulation experiments, finding that transport gaps could be tuned by varying the contact geometry [83]. Čerņevičs *et al.* investigated heterojunctions composed of graphene quantum dots embedded in metallic armchair graphene nanoribbon leads, revealing that the transport gap could be opened by adjusting both the width of the lead and the strength of the quantum dot-to-lead coupling [86]. However, borophene heterostructures and the impact of contacts on the electron transport properties of BNRs remain inadequately explored.

Building upon the successful experimental synthesis of several borophene heterostructures [71–74], we theoretically study the contact effects on the electron transport in two-terminal disordered BNRs with a random distribution of LDs by considering inhomogeneous model parameters, as illustrated in Fig. 1. Here, the source and the drain are chosen from the following four semi-infinite electrodes: the  $\nu_{1/6}$  BNR, the  $\nu_{1/5}$  BNR, the  $\nu_{1/3}$  BNR, and the square lattice (SL), as shown in Figs. 1(b)–1(e). We then discuss all these possible contact configurations. Notice that the  $\nu_{1/6}$  and  $\nu_{1/5}$  borophenes are prepared on Ag(111) substrate, whereas the  $\nu_{1/3}$  one of honeycomb, graphene-like structure has been successfully synthesized on Al(111) substrate in experiments [39]. The contact between the  $\nu_{1/6}$  ( $\nu_{1/5}$ ) borophene and the  $\nu_{1/3}$  one may then be realized by two alternative ways. First, after the isolation from Ag(111) substrate by using adhesive pads

[35], the  $\nu_{1/6}$  ( $\nu_{1/5}$ ) borophene will be placed nearby the  $\nu_{1/3}$  borophene grown on Al(111) substrate. These two different borophenes can then be stitched together by utilizing molecular beam epitaxy [14,15] or cluster expansion methods [34]. Second, after the independent preparation of the  $\nu_{1/6}$  ( $\nu_{1/5}$ ) borophene on Ag(111) substrate and the  $\nu_{1/3}$  one on Al(111) substrate, these two substrates will be combined laterally and separated by an ultrathin insulating layer so that the two different borophenes cannot interplay. By injecting sufficient boron atoms, the  $\nu_{1/6}$  ( $\nu_{1/5}$ ) and  $\nu_{1/3}$  borophenes could then be coupled and the contact appears. In contrast, the SL electrode is different from all the  $\nu_{1/6}$ ,  $\nu_{1/5}$ , and  $\nu_{1/3}$  BNRs, and it does not correspond to any actual borophene structure. Notice that many transport experiments are performed by taking normal metals as the electrodes, which are coupled directly to the two ends of measured materials of, e.g., graphene [2,3]. In this situation, the SL can be used to simulate these normal-metal electrodes, because the SL exhibits metallic behavior as normal metals. For instance, in previous transport works where graphene is coupled to normal metals, the SL electrode has been widely employed to describe normal metals instead of the contact between normal metals and graphene [76,77,82,84,89,90]. The SL electrode can also be described by the tight-binding model shown in Eq. (1).

Our results indicate that despite the substantial reduction in the overall conductance of disordered BNRs, several resonant peaks still appear in the transmission spectra, even in the presence of inhomogeneous tight-binding parameters. More importantly, the profile and amplitude of these resonant peaks at different electron energies can be declined to varying degrees for specific contact configurations, providing an essential aspect of tunability to this system. The amplitude of all the resonant peaks is exactly equal to the conductance quantum  $G_0$ , whereas the profile of certain specific resonant peaks undergoes unique changes when utilizing the  $\nu_{1/5}$  or  $\nu_{1/6}$  BNR as the electrodes. However, the amplitude of the resonant peaks exhibits varying degrees of reduction when the  $\nu_{1/3}$  BNR or the SL is taken as the electrodes, which contradicts the common belief that the amplitude of resonant peaks should strictly align with the conductance quantum  $G_0$ . Particularly, the resonant peaks for the contact configuration of the  $\nu_{1/3}$  BNR can be categorized into three types: weakly suppressed, partially suppressed, and completely suppressed. Through the analysis of the spatial distributions of bond currents in the system, we have provided explanations for the formation of these three types of resonant peaks. Moreover, the number of resonant peaks also increases with the width of the nanoribbons. We show that identical resonant peaks in disordered BNRs can evolve with varying widths, regardless of the contact configurations.

The remaining sections of the paper are organized as follows. Section II introduces the model Hamiltonian and Green's function utilized for calculating the conductance and the local bond currents distribution in the two-terminal disordered BNRs. Section III presents the results and discussion. Specifically, Sec. III A examines the contact effects on the electron transport in disordered BNRs, Sec. III B investigates the size-dependent electron transport in disordered BNRs, Sec. III C studies the conductance fluctuations and the localization in disordered BNRs, Sec. III D discusses the physical

origin of the different resonant peaks caused by the  $\nu_{1/3}$  BNR electrode, and Sec. III E explores the evolution of identical resonant peaks in disordered BNRs with different widths. Finally, the findings are summarized in Sec. IV.

## II. MODEL AND METHOD

The Hamiltonian that describes the electron transport in two-terminal disordered BNRs can be expressed as follows [47,48]:

$$\mathcal{H} = \sum_i \epsilon_i a_i^\dagger a_i - \sum_{\langle ij \rangle} t_{ij} a_i^\dagger a_j. \quad (1)$$

Here,  $a_i^\dagger$  ( $a_i$ ) represents the creation (annihilation) operator at site  $i$ . The term  $\epsilon_i$  signifies the on-site energy at site  $i$ , while  $t_{ij}$  denotes the nearest-neighbor hopping integral between sites  $i$  and  $j$ .

The two-terminal disordered BNRs can be separated into three subsystems, i.e., the source electrode ( $l < 1$ ), the central scattering region (CSR) ( $1 \leq l \leq L$ ), and the drain electrode ( $l > L$ ), as shown in Fig. 1(a). Here,  $l$  represents the chain index, and  $L$ , defined as the number of chains in the CSR, denotes the length of disordered BNRs. Thus the matrix form of the Hamiltonian described by Eq. (1) reads

$$\mathbf{H} = \begin{pmatrix} \mathbf{H}_S & \mathbf{h}_{Sc} & \mathbf{0} \\ \mathbf{h}_{Sc}^\dagger & \mathbf{H}_c & \mathbf{h}_{cD} \\ \mathbf{0} & \mathbf{h}_{cD}^\dagger & \mathbf{H}_D \end{pmatrix}. \quad (2)$$

Here,  $\mathbf{H}_c$  is the Hamiltonian of the CSR and can be expressed as follows:

$$\mathbf{H}_c = \begin{pmatrix} \mathbf{h}_{1,1} & \mathbf{h}_{1,2} & & \mathbf{0} \\ \mathbf{h}_{1,2}^\dagger & \mathbf{h}_{2,2} & \ddots & \\ & \ddots & \ddots & \mathbf{h}_{L-1,L} \\ \mathbf{0} & & & \mathbf{h}_{L,L}^\dagger \end{pmatrix}, \quad (3)$$

$\mathbf{H}_S$  ( $\mathbf{H}_D$ ) is the Hamiltonian of the source and drain, and  $\mathbf{h}_{Sc}$  ( $\mathbf{h}_{cD}$ ) represents the coupling Hamiltonian between the source (drain) and the CSR. Furthermore,  $\mathbf{h}_{l,l}$  is the sub-Hamiltonian of the  $l$ th chain, and  $\mathbf{h}_{l-1,l}$  is the coupling Hamiltonian between the  $(l-1)$ th chain and the  $l$ th chain.

By employing the Landauer-Büttiker formula together with the Green's function method, the conductance of the two-terminal disordered BNRs is written as

$$G = \frac{2e^2}{h} \text{Tr} (\mathbf{\Gamma}_S \mathbf{G}_c^r \mathbf{\Gamma}_D \mathbf{G}_c^a). \quad (4)$$

Here,  $\mathbf{\Gamma}_{S/D} = i(\mathbf{\Sigma}_{S/D}^r - \mathbf{\Sigma}_{S/D}^a)$  is the linewidth function.  $\mathbf{G}_c^r(E) = [\mathbf{G}_c^a(E)]^\dagger$  is the exact retarded Green's functions of this system and reads

$$\mathbf{G}_c^r(E) = (E\mathbf{I} - \mathbf{H}_c - \mathbf{\Sigma}_S^r - \mathbf{\Sigma}_D^r)^{-1}, \quad (5)$$

with  $E$  the electron energy and  $\mathbf{\Sigma}_{S/D}^r$  the retarded self-energy owing to the coupling to the source and drain, which is written as

$$\mathbf{\Sigma}_S^r = \mathbf{h}_{Sc}^\dagger \mathbf{g}_S^r \mathbf{h}_{Sc}, \quad (6a)$$

$$\mathbf{\Sigma}_D^r = \mathbf{h}_{cD}^\dagger \mathbf{g}_D^r \mathbf{h}_{cD}, \quad (6b)$$

where  $\mathbf{g}_{S/D}^r$  is the retarded surface Green's function of the semi-infinite source/drain electrode, which can be calculated by using the iterative scheme [91,92]. To circumvent the direct calculation of conductance from Eq. (4), we employ the recursive Green's function method [93], where the conductance in Eq. (4) can be rewritten as

$$G = \frac{2e^2}{h} \text{Tr} [(\Gamma_S)_{1,1}(\mathbf{G}_c^r)_{1,L}(\Gamma_D)_{L,L}(\mathbf{G}_c^a)_{L,1}], \quad (7)$$

where  $(\mathbf{G}_c^r)_{1,L}$  is the submatrix of  $\mathbf{G}_c^r$  [93]. Furthermore, the bond currents flowing between the  $j$ th site of the  $l$ th chain and the  $j'$ th site of the  $l'$ th chain are as follows:

$$I_{(l,j) \rightarrow (l',j')} = -\frac{2e}{h} \int dE [\mathbf{h}_{l,l'}(j, j') (\mathbf{G}_c^<)_{l,l'}(j', j) - \mathbf{h}_{l',l}(j', j) (\mathbf{G}_c^<)_{l,l'}(j, j')], \quad (8)$$

where  $(\mathbf{G}_c^<)_{l,l'}$  is the submatrix of exact lesser Green's function  $\mathbf{G}_c^<$ .

To derive the submatrices of  $\mathbf{G}_c^r$  and  $\mathbf{G}_c^<$ , we employ a recurrence formula that utilizes the Green's function obtained from both left-to-right and right-to-left sweeps. In accordance with the Dyson equation, the retarded Green's function at the first chain, obtained from the left-to-right sweep, is given by

$$(\mathbf{G}_c^r)_{1,1}^{L \rightarrow R} = [\mathbf{E}\mathbf{I} - \mathbf{h}_{1,1} - (\Sigma_S^r)_{1,1}]^{-1}. \quad (9)$$

Here, the superscripts  $L \rightarrow R$  and  $R \rightarrow L$  signify the left-to-right and right-to-left sweeps, respectively. Then, for the  $l$ th ( $l \in [2, L-1]$ ) chain

$$(\mathbf{G}_c^r)_{l,l}^{L \rightarrow R} = [\mathbf{E}\mathbf{I} - \mathbf{h}_{l,l} - \mathbf{h}_{l-1,l}^\dagger (\mathbf{G}_c^r)_{l-1,l-1}^{L \rightarrow R} \mathbf{h}_{l-1,l}]^{-1}, \quad (10a)$$

$$(\mathbf{G}_c^r)_{1,l}^{L \rightarrow R} = (\mathbf{G}_c^r)_{1,l-1}^{L \rightarrow R} \mathbf{h}_{l-1,l} (\mathbf{G}_c^r)_{l,l}^{L \rightarrow R}. \quad (10b)$$

According to the fluctuation-dissipation relations, the initial value lesser Green's function reads

$$(\mathbf{G}_c^<)_{0,0}^{L \rightarrow R} = \mathbf{g}_S^< = -f_S(\mathbf{g}_S^r - \mathbf{g}_S^a), \quad (11)$$

where  $f_S$  and  $f_D$  denote the Fermi distributions in the source and drain electrodes, respectively. Utilizing the aforementioned equations, the lesser Green's function for each value of  $l$  obtained from a left-to-right sweep can be further derived as follows:

$$(\mathbf{G}_c^<)_{l,l}^{L \rightarrow R} = (\mathbf{G}_c^r)_{l,l}^{L \rightarrow R} (\Sigma^<)_{l,l}^{L \rightarrow R} (\mathbf{G}_c^a)_{l,l}^{L \rightarrow R}. \quad (12)$$

Here,  $(\Sigma^<)_{l,l}^{L \rightarrow R}$  represents the self-energy arising from the coupling of the  $l$ th chain to all other chains on its left and reads

$$(\Sigma^<)_{l,l}^{L \rightarrow R} = \mathbf{h}_{l-1,l}^\dagger (\mathbf{G}_c^<)_{l-1,l-1}^{L \rightarrow R} \mathbf{h}_{l-1,l}. \quad (13)$$

For the right-to-left sweep, similarly we have

$$(\mathbf{G}_c^r)_{L,L}^{R \rightarrow L} = [\mathbf{E}\mathbf{I} - \mathbf{h}_{L,L} - (\Sigma_D^r)_{L,L}]^{-1}. \quad (14)$$

Then, the submatrices  $(\mathbf{G}_c^r)_{l,l}^{R \rightarrow L}$  can be calculated from the recursive equations:

$$(\mathbf{G}_c^r)_{l,l}^{R \rightarrow L} = [\mathbf{E}\mathbf{I} - \mathbf{h}_{l,l} - \mathbf{h}_{l+1,l} (\mathbf{G}_c^r)_{l+1,l+1}^{R \rightarrow L} \mathbf{h}_{l+1,l}^\dagger]^{-1}. \quad (15)$$

Likely, the initial value of lesser Green's function in the right-to-left sweep reads

$$(\mathbf{G}_c^<)_{L+1,L+1}^{R \rightarrow L} = \mathbf{g}_D^< = -f_D(\mathbf{g}_D^r - \mathbf{g}_D^a). \quad (16)$$

The lesser Green's function for the  $l$ th chain obtained from right-to-left sweep reads

$$(\mathbf{G}_c^<)_{l,l}^{R \rightarrow L} = (\mathbf{G}_c^r)_{l,l}^{R \rightarrow L} (\Sigma^<)_{l,l}^{R \rightarrow L} (\mathbf{G}_c^a)_{l,l}^{R \rightarrow L}. \quad (17)$$

Here,  $(\Sigma^<)_{l,l}^{R \rightarrow L}$  represents the self-energy arising from the coupling of the  $l$ th chain to all other chains on its right and reads

$$(\Sigma^<)_{l,l}^{R \rightarrow L} = \mathbf{h}_{l+1,l} (\mathbf{G}_c^<)_{l+1,l+1}^{R \rightarrow L} \mathbf{h}_{l+1,l}^\dagger. \quad (18)$$

Combining the Green's functions obtained from two sweeps, the exact retarded Green's functions for the  $l$ th chain are given by

$$(\mathbf{G}_c^r)_{l,l} = [\mathbf{E}\mathbf{I} - \mathbf{h}_{l,l} - \mathbf{h}_{l-1,l}^\dagger (\mathbf{G}_c^r)_{l-1,l-1}^{L \rightarrow R} \mathbf{h}_{l-1,l} - \mathbf{h}_{l+1,l} (\mathbf{G}_c^r)_{l+1,l+1}^{R \rightarrow L} \mathbf{h}_{l+1,l}^\dagger]^{-1}. \quad (19)$$

Specifically, the exact retarded Green's function of the  $L$ th (1st) chain can be directly determined by employing a left-to-right (or right-to-left) sweep, given that the self-energy of the source and drain electrodes is already known

$$(\mathbf{G}_c^r)_{L,L} = [\mathbf{E}\mathbf{I} - \mathbf{h}_{L,L} - \mathbf{h}_{L-1,L}^\dagger (\mathbf{G}_c^r)_{L-1,L-1}^{L \rightarrow R} \mathbf{h}_{L-1,L} - (\Sigma_D^r)_{L,L}]^{-1}, \quad (20a)$$

$$(\mathbf{G}_c^r)_{1,1} = [\mathbf{E}\mathbf{I} - \mathbf{h}_{1,1} - \mathbf{h}_{1,2} (\mathbf{G}_c^r)_{2,2}^{R \rightarrow L} \mathbf{h}_{1,2}^\dagger - (\Sigma_S^r)_{1,1}]^{-1}. \quad (20b)$$

Then, we have

$$(\mathbf{G}_c^r)_{1,L} = (\mathbf{G}_c^r)_{1,L-1}^{L \rightarrow R} \mathbf{h}_{L-1,L} (\mathbf{G}_c^r)_{L,L}, \quad (21)$$

and the conductance in Eq. (7) can be directly obtained from left-to-right sweep. The exact lesser Green's function of the  $l$ th chain reads

$$(\mathbf{G}_c^<)_{l,l} = (\mathbf{G}_c^r)_{l,l} [(\Sigma^<)_{l,l}^{L \rightarrow R} + (\Sigma^<)_{l,l}^{R \rightarrow L}] (\mathbf{G}_c^a)_{l,l}. \quad (22)$$

Finally, we obtain the exact inter-chain lesser Green's functions by applying the Dyson-Langreth equations [94]:

$$(\mathbf{G}_c^<)_{l-1,l} = (\mathbf{G}_c^r)_{l-1,l-1}^{L \rightarrow R} \mathbf{h}_{l-1,l} (\mathbf{G}_c^<)_{l,l} + (\mathbf{G}_c^<)_{l-1,l-1}^{L \rightarrow R} \mathbf{h}_{l-1,l} (\mathbf{G}_c^a)_{l,l}, \quad (23a)$$

$$(\mathbf{G}_c^<)_{l,l-1} = (\mathbf{G}_c^r)_{l,l} \mathbf{h}_{l-1,l}^\dagger (\mathbf{G}_c^<)_{l-1,l-1}^{L \rightarrow R} + (\mathbf{G}_c^<)_{l,l} \mathbf{h}_{l-1,l}^\dagger (\mathbf{G}_c^a)_{l-1,l-1}^{L \rightarrow R}. \quad (23b)$$

Substituting Eqs. (22), (23a), and (23b) into Eq. (8) yields the current density distribution of the system.

### III. RESULTS AND DISCUSSION

For the disordered BNRs in the CSR, we consider the length of  $L = 4000$  with the ratio of the (2, 2) chain to the (2, 3) one setting to 1:1. According to the experiments [15], the width of BNRs is estimated to be  $0.15N$  nm and it is about 4.35 nm for  $N = 29$ . The conductance is averaged over 2000 disordered samples, unless stated otherwise. We systematically investigate all the possible contact configurations, representing them as [source electrode, drain electrode]. For instance,  $[\nu_{1/5}, \nu_{1/6}]$  denotes the contact configuration where

TABLE I. The on-site energy  $\epsilon_i$  and the hopping integral  $t_{ij}$  dependent on the number of adjacent atoms  $\xi_i$  [47,48].

$\xi_i$	$\epsilon_i$	$t_{ij}(\xi_j = 4)$	$t_{ij}(\xi_j = 5)$	$t_{ij}(\xi_j = 6)$
4	$-0.098t$	$1.06t$	$1.02t$	$0.895t$
5	$0.029t$	$1.02t$	$0.955t$	$0.92t$
6	$0.4225t$	$0.895t$	$0.92t$	

the source and drain electrodes are the  $\nu_{1/5}$  and  $\nu_{1/6}$  BNRs, respectively. We emphasize that the exchange of the source and drain electrodes does not alter the calculated results due to the time-reversal symmetry.

The inhomogeneous tight-binding parameters with inversion symmetry for the  $\nu_{1/5}$  and  $\nu_{1/6}$  BNRs are derived from first-principles calculations, and their values are determined by the number of adjacent atoms [47,48]. Here, we define  $\xi_i$  as the number of adjacent atoms at site  $i$ . Notably, the on-site energy  $\epsilon_i$  depends on  $\xi_i$ , while the hopping integral  $t_{ij}$  depends on both  $\xi_i$  and  $\xi_j$ , as detailed in Table I. As illustrated in Figs. 1(f) and 1(g), the value of  $\xi_i$  is 4 for atoms labeled with the letters a, e, u, and x, 5 for atoms labeled with the letters b, d, v, and w, and 6 for atom labeled with the letter c. The on-site energy and the hopping integral in the  $\nu_{1/3}$  BNR and the SL electrode are set to  $\epsilon_i = 0$  and  $t_{ij} = t$ , as each atom has an equal number of neighbors. The CSR and the  $\nu_{1/3}$  BNR or the SL electrode hopping integrals are denoted as  $t$  without loss of generality.

### A. Contact effects on the electron transport in disordered BNRs

To understand the distinctions among these electrodes, we initially study the electron transport properties of various periodic BNRs. Figure 2(a) shows the conductance  $G$  as a function of energy  $E$  for periodic  $\nu_{1/5}$  BNR,  $\nu_{1/6}$  BNR, and  $\nu_{1/3}$  BNR, respectively, with size  $N = 29$  and  $L = 4000$ . The transmission spectra of these periodic BNRs share some common characteristics. First, all these periodic BNRs exhibit metallic behavior, in agreement with experimental observations [15,39]. Second, the transmission spectra of these periodic BNRs are characterized by numerous quantized conductance plateaus with integer multiples of  $G_0 = 2e^2/h$ . It is worth noting that the positions of these conductance plateaus for the  $\nu_{1/5}$  and  $\nu_{1/6}$  BNRs with inhomogeneous parameters are shifted as compared with those of homogeneous parameters [64]. Meanwhile, noticeable disparities in the transmission spectra are apparent. In case of the  $\nu_{1/3}$  BNR, the  $G - E$  curve exhibits symmetry with respect to the line  $E = 0$ , attributed to the preservation of the electron-hole symmetry, consistent with graphene [2]. As the electron energy deviates from  $E = 0$ , the conductance plateaus increase monotonously [see the blue-solid line in Fig. 2(a)]. For the  $\nu_{1/5}$  and  $\nu_{1/6}$  BNRs, their  $G - E$  curves exhibit asymmetry with respect to the line  $E = 0$  [see the black-solid and red-solid lines in Fig. 2(a)], owing to the breaking of the electron-hole symmetry. The conductance plateaus of the  $\nu_{1/5}$  and  $\nu_{1/6}$  BNRs exhibit non-monotonic variations as  $E$  deviates from  $E = 0$ , resulting in multiple conductance dips. For example, the conductance dips are observed in the vicinity of  $E = 0$  and  $E = -0.6t$  for the  $\nu_{1/6}$  BNR, as indicated by the magenta and green

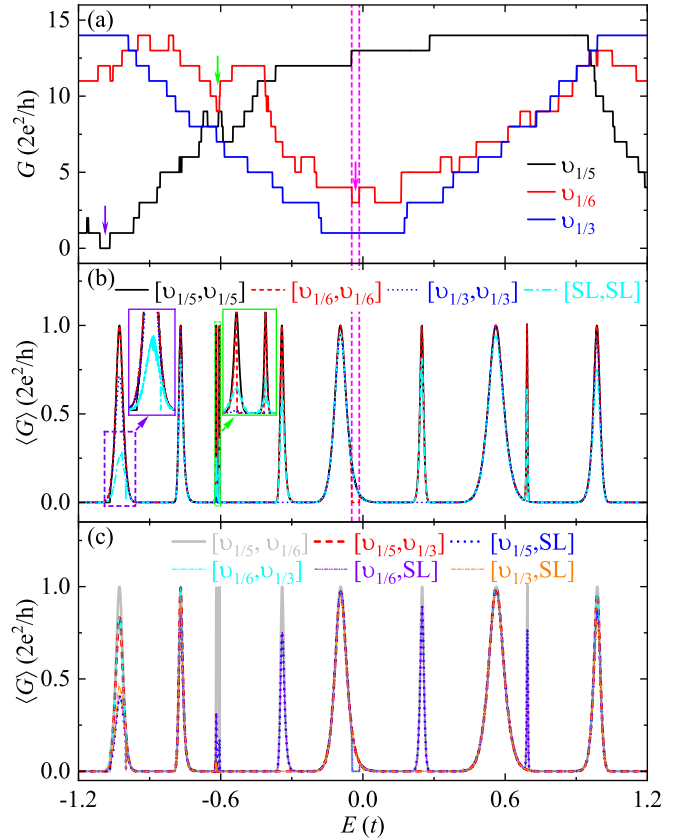


FIG. 2. Electron transport along the periodic and disordered BNRs under different contact configurations. (a) Energy-dependent conductance  $G$  for periodic  $\nu_{1/5}$  BNR,  $\nu_{1/6}$  BNR, and  $\nu_{1/3}$  BNR. Energy-dependent averaged conductance  $\langle G \rangle$  for disordered BNRs with (b) identical and (c) different source and drain electrodes. The left inset in (b) provides an enlarged image of the resonant peak at  $E = -1.027t$ . The right inset in (b) provides an enlarged image of the line-type resonant peaks at  $E \sim -0.605t$ , and  $-0.619t$ . Here,  $N = 29$ .

arrows in Fig. 2(a), respectively. Additionally, a conductance dip emerges around  $E = -t$  for the  $\nu_{1/5}$  BNR, as shown by the violet arrow in Fig. 2(a). These unnoticed conductance dips reveal the absence of electron-transport modes and may lead to distinct transport properties for the contact configuration of the  $\nu_{1/5}$  and  $\nu_{1/6}$  BNRs.

Figure 2(b) shows the averaged conductance  $\langle G \rangle$  versus  $E$  for disordered BNRs under the contact configurations where the source electrode is the same as the drain one. There are four contact configurations, namely  $[\nu_{1/6}, \nu_{1/6}]$ ,  $[\nu_{1/5}, \nu_{1/5}]$ ,  $[\nu_{1/3}, \nu_{1/3}]$ , and  $[\text{SL}, \text{SL}]$ . For all these contact configurations, it is clear that the overall conductance is notably suppressed as anticipated, owing to the successive scattering caused by random LDs. However, numerous transmission peaks with varying full widths at half maximum (FWHM) emerge in the transmission spectrum due to the resonant tunneling [64]. In contrast to the resonant tunneling observed in disordered BNRs with homogeneous parameters, substantial alterations take place in the numbers, positions, and profiles of resonant peaks. Specifically, multiple line-type resonant peaks with very small FWHM emerge, exemplified by the resonant

peaks at  $E \sim -0.605t$  and  $-0.619t$ . Unlike the line-type resonant peaks in Dirac materials of graphene [95] and WSe<sub>2</sub> superlattices [96] that appear dependent to the angle of incident electrons, the line-type resonant peaks in disordered BNRs maintaining consistent positions in all these contact configurations. Indeed, the positions of all the resonant peaks remain unaffected by changes in the contact configurations, as they are inherently determined by the disordered BNR in the CSR. Nevertheless, the profile and amplitude of these resonant peaks are notably affected by changes in the contact configurations.

Specifically, in the contact configurations [ $\nu_{1/5}, \nu_{1/5}$ ] and [ $\nu_{1/6}, \nu_{1/6}$ ], all the resonant peaks exhibit a consistent amplitude of  $\langle G \rangle = G_0$  [see the black-solid and red-dashed lines in Fig. 2(b)]. Since both  $\nu_{1/6}$  and  $\nu_{1/5}$  BNRs consist of (2, 2) and (2, 3) chains, they possess identical resonant states with the disordered BNRs in the CSR, and no interface scattering occurs, as further demonstrated in Fig. 5. However, the profile of some special resonant peaks is different between these two contact configurations. In the contact configuration [ $\nu_{1/6}, \nu_{1/6}$ ], a portion conductance on the right side of the resonant peak at  $E \sim -0.095t$  disappears, and a small transmission gap emerges [see the red-dashed line in Fig. 2(b)]. When revisiting the transmission spectrum of the periodic  $\nu_{1/6}$  BNR, a previously mentioned conductance dip around  $E = 0$  can be found, as indicated by the magenta-dashed lines in Figs. 2(a) and 2(b). The conductance of the right part of the line-type resonant peak at  $E \sim -0.619t$  and the left part of the line-type resonant peak at  $E \sim -0.605t$  disappears, enlarging the transmission gap between these two line-type resonant peaks [see the red-dashed line in the right inset of Fig. 2(b)]. The energy range of the enlarged transmission gap is equal to that of the conductance dip around  $E \sim -0.6t$  in the transmission spectrum of the periodic  $\nu_{1/6}$  BNR. Furthermore, the conductance switches between  $G_0$  and 0 as  $E$  increases from  $-0.619t$  to  $-0.605t$ , implying the potential utility of disordered BNRs as electron energy filters. In the contact configuration [ $\nu_{1/5}, \nu_{1/5}$ ], similarly, a portion conductance on the left side of the resonant peak at  $E \sim -1.027t$  disappears [see the black-solid line in the left inset of Fig. 2(b) for clarification]. One can also observe a conductance dip appearing around  $E = -t$  in the transmission spectrum of the periodic  $\nu_{1/5}$  BNR [see the violet arrow in Fig. 2(a)]. Consequently, the contact effects induced by the  $\nu_{1/5}$  and  $\nu_{1/6}$  BNRs, influencing the profile of the resonant peaks, can be linked to the conductance dip in their periodic counterparts, arising from the absence of electron-transport modes in the vicinity of the resonant energy.

The contact effects become more significant in the contact configurations [ $\nu_{1/3}, \nu_{1/3}$ ] or [SL, SL]. A comparison with the contact configurations [ $\nu_{1/5}, \nu_{1/5}$ ] and [ $\nu_{1/6}, \nu_{1/6}$ ] reveals that the amplitude of all the resonant peaks is less than  $G_0$ , and the magnitude of this reduction is dependent on the resonant energy [see the blue-dotted and cyan-dashed-dotted lines in Fig. 2(b)]. In particular, the resonant peaks in the contact configurations [ $\nu_{1/3}, \nu_{1/3}$ ] can be divided into three classes. (i) The resonant peaks at energies  $E \sim 0.693t, 0.249t$ , and  $-0.342t$  as well as the line-type one at  $-0.605t$  are completely suppressed. (ii) The resonant peak at  $E \sim -1.027t$  and the line-type one at  $-0.619t$  are strongly suppressed with

$\langle G \rangle \sim 0.717G_0$  and  $0.025G_0$ , respectively. (iii) The resonant peaks at  $E \sim -0.769t, -0.095t$ , and  $0.561t$  are weakly suppressed, with the amplitude approaching  $G_0$ . These results suggest that the  $\nu_{1/3}$  BNR can effectively serve as a selective filter for specific resonant peaks, which we refer to as the resonant peak filtering effect. In the contact configuration [SL, SL], each resonant peak experiences varying degrees of suppression compared to the [ $\nu_{1/3}, \nu_{1/3}$ ]. In particular, the resonant peak at  $E \sim -1.027t$  exhibits pronounced oscillations and has the amplitude of  $0.270G_0$ , which is smaller than that of the [ $\nu_{1/3}, \nu_{1/3}$ ] [see the cyan-dashed-dotted line in the left inset of Fig. 2(b)]. However, none of them are completely suppressed, implying that the resonant peak filtering effect is a unique characteristic of the  $\nu_{1/3}$  BNR electrode. In contrast to the contact configurations [ $\nu_{1/5}, \nu_{1/5}$ ] and [ $\nu_{1/6}, \nu_{1/6}$ ], there is no observable conductance dip in the transmission spectrum of the  $\nu_{1/3}$  BNR [see the blue-solid line in Fig. 2(a)].

The variation in the amplitude of resonant peaks for different contact configurations can be attributed to distinct scattering probability at the interface between different electrodes and the CSR. Although all the electrodes are metallic, their electron-transport modes are different. When the electrodes are taken as either the  $\nu_{1/6}$  BNR or the  $\nu_{1/5}$  one, the electron-transport modes in the electrodes are identical to those in the CSR and no scattering occurs at the electrode-CSR interface, because the CSR is composed of many  $\nu_{1/6}$  and  $\nu_{1/5}$  BNRs. In this situation, the amplitude of resonant peaks is exactly the conductance quantum  $G_0$ . By contrast, when the electrodes are taken as either the  $\nu_{1/3}$  BNR or the SL, the electron-transport modes mismatch with those in the CSR and the scattering takes place at the interface. Then, the amplitude is less than  $G_0$  and some resonant peaks can even disappear when the  $\nu_{1/3}$  BNR or the SL is chosen as the electrodes. Similarly, when transition metals are used as the electrodes, the amplitude of resonant peaks will be declined and some resonant peaks may even vanish, because the electron-transport modes of transition metals is different from those in the CSR due to distinct lattice structures. The physical origin of the resonant peak filtering effect will be further discussed later.

We then consider contact configurations with distinct source and drain electrodes, resulting in six unique contact configurations. The corresponding  $\langle G \rangle - E$  curves are depicted in Fig. 2(c), and the main results can be summarized as follows: (i) The discussed contact effects are effective in the contact configurations with different source and drain electrodes. For example, the specific profile of resonant peak at  $E \sim -0.095t$  is observed in the transmission spectra for the contact configurations where one of the electrodes is the  $\nu_{1/6}$  BNR [see the gray-solid, cyan-dashed-dotted, and violet-dashed-dotted-dotted lines in Fig. 2(c)]. Resonant peak filtering effect appears in the transmission spectra for the contact configurations where one of the electrodes is the  $\nu_{1/3}$  BNR [see the red-dashed, cyan-dashed-dotted, and orange-dashed-dotted-dotted lines in Fig. 2(c)]. The resonant peak at  $E \sim -1.027t$  becomes high oscillations in the transmission spectra for the contact configurations where one of the electrodes is the SL [see the blue-dotted, violet-dashed-dotted-dotted, and orange-dashed-dashed-dotted lines in Fig. 2(c)]. (ii) Different contact effects are cumulative when considering distinct source and drain electrodes. For instance, in the contact

TABLE II. The amplitude of the resonant peak  $\langle G \rangle$  at  $E \sim -1.027t$  dependent on the contact configurations.

contact configuration	$\langle G \rangle (E \sim -1.027t)$
$[\nu_{1/5}, \nu_{1/5}], [\nu_{1/6}, \nu_{1/6}], [\nu_{1/5}, \nu_{1/6}]$	$G_0$
$[\nu_{1/3}, \nu_{1/3}]$	$0.717G_0$
[SL, SL]	$0.270G_0$
$[\nu_{1/5}, \nu_{1/3}], [\nu_{1/6}, \nu_{1/3}]$	$0.834G_0$
$[\nu_{1/5}, \text{SL}], [\nu_{1/6}, \text{SL}]$	$0.510G_0$
$[\nu_{1/3}, \text{SL}]$	$0.471G_0$

configuration  $[\nu_{1/5}, \nu_{1/6}]$ , the resonant peak at  $E \sim -1.027t$  has the same profile as that of  $[\nu_{1/5}, \nu_{1/5}]$ , while the resonant peak at  $E \sim -0.095t$  has the same profile as that of  $[\nu_{1/6}, \nu_{1/6}]$  [see the gray-solid line in Fig. 2(c)]. In the contact configuration  $[\nu_{1/6}, \nu_{1/3}]$ , the resonant peak filtering effect evidently appears as that of  $[\nu_{1/3}, \nu_{1/3}]$ , and the resonant peak at  $E \sim -0.095t$  has the same profile as that of  $[\nu_{1/6}, \nu_{1/6}]$  [see the cyan-dashed-dotted line in Fig. 2(c)]. (iii) Considering distinct source and drain electrodes allows for tuning the amplitude of resonant peaks into a broader range. Clearly, the amplitude of the resonant peak at  $E \sim -1.027t$  can be varied across six different values by altering the contact configurations, as summarized in Table II. This indicates that the reduction in the amplitude of the resonant peaks is attributed to the interface scattering between the CSR and the SL electrode or the  $\nu_{1/3}$  BNR electrode. At  $E \sim -1.027t$ , the former interface scattering strength surpasses the latter, and the amplitude of the resonant peaks varies with changes in the number of the SL electrode and the  $\nu_{1/3}$  BNR electrode. Consequently, choosing different electrodes for the source and the drain enables simultaneous and distinct control over the electron transport through disordered BNRs.

### B. Contact effects on the electron transport in disordered BNRs of varying sizes

Next, we investigate the contact effects on the electron transport in disordered BNRs with different sizes. In the following section, our primary focus will be on the two contact configurations:  $[\nu_{1/6}, \nu_{1/6}]$  and  $[\nu_{1/5}, \nu_{1/3}]$ . Figure 3(a) shows  $\langle G \rangle$  vs  $E$  for disordered BNRs with different widths  $N$  in the contact configuration  $[\nu_{1/6}, \nu_{1/6}]$ . Clearly, resonant peaks with amplitude  $G = G_0$  are observed across various widths, emphasizing the resonant tunneling in disordered BNRs. With  $N$  varying from 2 to 36, the total number of resonant peaks increases due to the rising density of resonant states in disordered BNRs. The subsequent discussion in Sec. III E covers the underlying evolution of resonant peaks in disordered BNRs with different  $N$ . However, there are some features that warrant attention here. For  $N = 2$ , resonant peaks appear at  $E \sim -0.095t$  and  $-1.027t$ , with a small transmission gap for the peak at  $E \sim -0.095t$  [see the black-solid line in Fig. 3(a)]. Consistently, as previously discussed, two identical resonant peaks, featuring the same profile and amplitude, are consistently observed for  $N = 29$  at the same energy in the same contact configuration [see the red-dashed line in Fig. 2(b)]. The resonant peaks observed in the transmission spectrum of  $N = 4$  [see red-dashed line in Fig. 3(a)] are also discernible

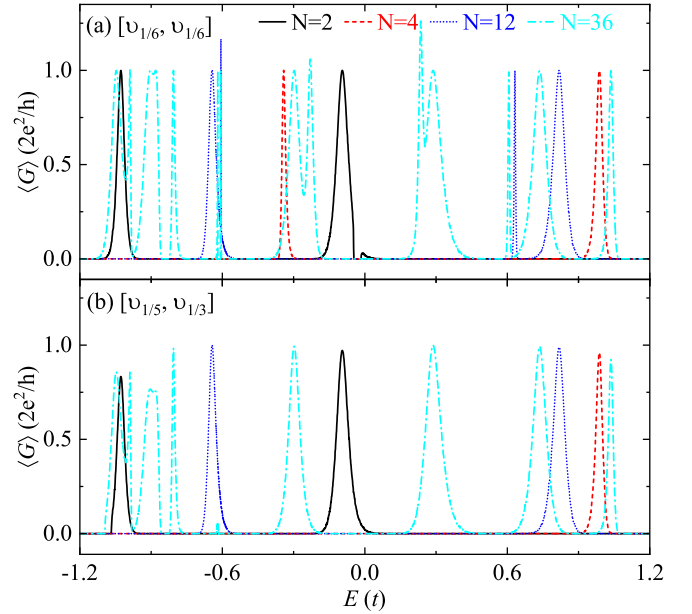


FIG. 3. Electron transport through disordered BNRs with different widths  $N$  for contact configurations (a)  $[\nu_{1/6}, \nu_{1/6}]$  and (b)  $[\nu_{1/5}, \nu_{1/3}]$ .

that of  $N = 29$ . Furthermore, the line-type resonant peaks are observed around  $E = -0.6t$  in disordered BNRs with  $N = 12$  and  $N = 36$ , like  $N = 29$  [see the blue-dotted and cyan-dashed-dotted lines in Fig. 3(a)], suggesting the presence of identical resonant peaks across different values of  $N$  in disordered BNRs. The presence of identical resonant peaks further suggests the consistency of contact effects on resonant peaks at the same energy in disordered BNRs with different  $N$ . For example, a transmission gap is observed for the resonant peak at  $E \sim -0.095t$  for the disordered BNRs with  $N = 2$  and  $29$ .

Figure 3(b) displays the same information as Fig. 3(a), but in the contact configuration  $[\nu_{1/5}, \nu_{1/3}]$ . Similar to the contact configuration  $[\nu_{1/6}, \nu_{1/6}]$ , the number and position of resonant peaks vary with  $N$ . Despite the larger number of resonant peaks in  $N = 2$  compared to  $N = 4$ , the overall count of resonant peaks rises with increasing  $N$ , as further illustrated in Fig. 9(b). The profile and amplitude of these resonant peaks are notably affected, owing to the contact effects of the  $\nu_{1/5}$  and  $\nu_{1/3}$  BNR electrodes. Likely, identical resonant peak also appears in disordered BNRs with different  $N$ . All the resonant peaks in disordered BNRs with  $N = 2$  and  $4$  [see the black-solid and red-dashed lines in Fig. 3(b)] can be found in the transmission spectrum of  $N = 29$  with the same contact configuration [see the red-dashed line in Fig. 2(c)], with the same profile and amplitude. Compared to the contact configuration  $[\nu_{1/6}, \nu_{1/6}]$ , the resonant peak at  $E \sim -0.342t$  in the disordered BNR with  $N = 4$  is filtered in the contact configuration  $[\nu_{1/5}, \nu_{1/3}]$ , similar to the identical one in  $N = 29$ , owing to the resonant peak filtering effect of the  $\nu_{1/3}$  BNR electrode. Furthermore, the resonant peak filtering effect of the  $\nu_{1/3}$  electrode is also observable in disordered BNRs with  $N = 12$  and  $N = 36$  [see the blue-dotted and cyan-dashed-dotted lines in Fig. 3(b)]. Consequently, the contact effects exert significant

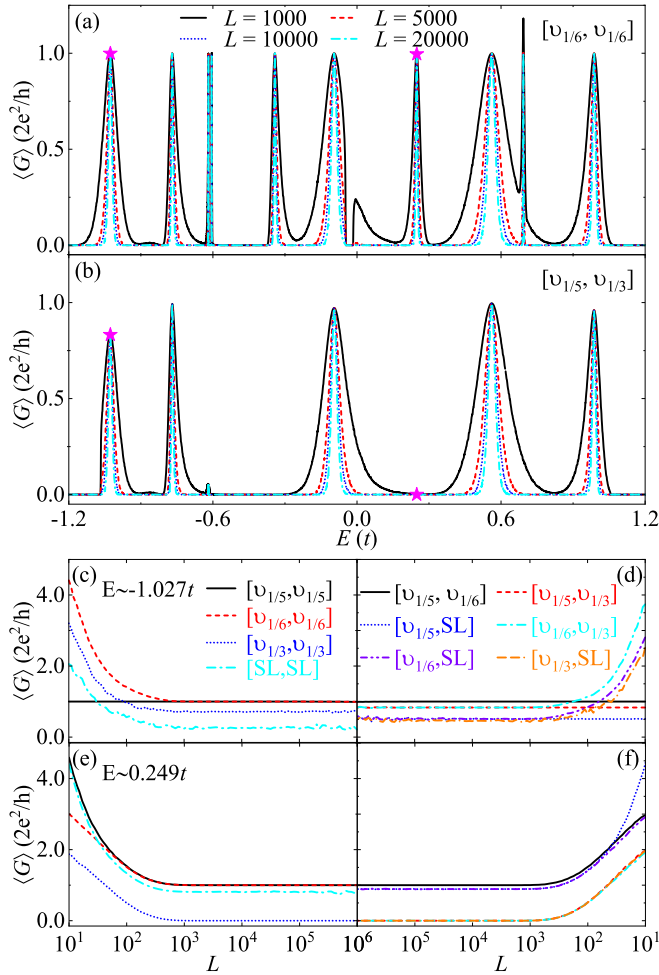


FIG. 4. Electron transport through disordered BNRs with varying length  $L$  for different contact configurations. (a) and (b) show  $\langle G \rangle$  as a function of energy  $E$  for different  $L$ , with contact configurations  $[\nu_{1/6}, \nu_{1/6}]$  and  $[\nu_{1/5}, \nu_{1/3}]$ , respectively. (c) and (d) depict  $\langle G \rangle$  vs  $L$  for contact configurations with identical and different source and drain electrodes at  $E \sim -1.027t$ , respectively. Similarly, (e) and (f) show the same as (c) and (d) but at  $E \sim 0.249t$ . Here,  $N = 29$ .

influence on the electron transport in disordered BNRs of varying widths.

Figures 4(a) and 4(b) depict  $\langle G \rangle$  as a function of  $E$  for disordered BNRs with length ranging from  $L = 1000$  to  $20\,000$  for the contact configurations  $[\nu_{1/6}, \nu_{1/6}]$  and  $[\nu_{1/5}, \nu_{1/3}]$ , respectively. Despite the suppression of the resonant peaks in disordered BNRs for the contact configuration  $[\nu_{1/5}, \nu_{1/3}]$ , the amplitude of the resonant peaks in both contact configurations remains constant with increasing  $L$ . This further indicates that the decrease of the peak amplitude is attributed to the interface scattering between the  $\nu_{1/3}$  BNR electrode and the CSR, irrespective of  $L$ . Furthermore, it highlights the robustness of resonant peaks and the existence of delocalized states in disordered BNRs, consistent with experimental observations [57]. For  $L = 1000$ , the resonant peaks in the transmission spectrum exhibit large FWHM [see the black-solid line in Figs. 4(a) and 4(b)]. Thus the profile of the resonant peaks at  $E \sim -0.095t$  and  $E \sim -1.027t$  due to the contact effects of the  $\nu_{1/5}$  and  $\nu_{1/6}$  BNR electrodes becomes

pronounced, respectively. By increasing the length from  $L = 1000$  to  $20\,000$ ,  $\langle G \rangle$  decreases at all the energies except for the resonant ones, resulting in a reduction of the FWHM for all the resonant peaks. For  $L = 10000$  and  $20\,000$ , the profile of the resonant peaks will not be affected by the absence of electron-transport modes in the  $\nu_{1/5}$  and  $\nu_{1/6}$  BNR electrodes, due to the significant reduction in the FWHM [see the blue-dotted and cyan-dashed-dotted lines in Figs. 4(a) and 4(b)]. Moreover, the resonant peak filtering effect of the  $\nu_{1/3}$  BNR electrode remains valid for all the values of  $L$  [see Fig. 4(b)].

To further investigate the length-dependent electron transport in disordered BNRs, Figs. 4(c) and 4(e) illustrate  $\langle G \rangle$  versus  $L$  at  $E \sim -1.027t$  and  $E \sim 0.249t$ , respectively, considering the contact configurations with identical source and drain electrodes. Here,  $E \sim -1.027t$  and  $0.249t$  [indicated by magenta stars in Figs. 4(a) and 4(b)] correspond to the resonant peaks that are strongly and completely suppressed by the  $\nu_{1/3}$  BNR electrode, respectively. The results are calculated from  $1 \times 10^7/L$  disordered samples. By examining Figs. 4(c) and 4(e), significant differences between various contact configurations in  $\langle G \rangle - L$  curves can be identified: (i) In the contact configuration  $[\nu_{1/5}, \nu_{1/5}]$ ,  $\langle G \rangle$  at the resonant energy of  $E \sim -1.027t$  consistently remains  $G_0$  regardless of  $L$  [see the black-solid line in Fig. 4(c)], as there exists only one electron-transport mode in the  $\nu_{1/5}$  electrode for  $E \sim -1.027t$  [see the black-solid line in Fig. 2(a)]. While for  $E \sim 0.249t$ ,  $\langle G \rangle$  decreases as  $L$  increases initially, eventually approaching  $G_0$  when  $L$  exceeds  $10^3$  [see the black-solid line in Fig. 4(e)]. (ii) In the contact configuration  $[\nu_{1/6}, \nu_{1/6}]$ ,  $\langle G \rangle$  at  $E \sim -1.027t$  and  $E \sim 0.249t$  decreases as the  $L$  increases, eventually approaching  $G_0$  when  $L$  exceeds  $10^3$  [see the red-dashed line in Figs. 4(c) and 4(e)]. (iii) For the contact configuration  $[\nu_{1/3}, \nu_{1/3}]$ ,  $\langle G \rangle$  at  $E \sim -1.027t$  is declined to  $0.717G_0$  when  $L > 10^3$ , and remains stable further with a continued increase in  $L$  to  $L > 10^6$  [see the blue-dotted line in Fig. 4(c)]. While  $\langle G \rangle$  at  $E \sim 0.249t$  is directly declined to 0 when  $L$  exceeds  $10^3$  due to the resonant peaks filtering effect [see the blue-dotted line in Fig. 4(e)]. (iv) For the contact configuration  $[SL, SL]$ ,  $\langle G \rangle$  at  $E \sim -1.027t$  and  $0.249t$  decreases to a value smaller than  $G_0$  when  $L > 10^3$ , and also remains stable by further increasing  $L$  [see the cyan-dash-dotted line in Figs. 4(c) and 4(e)]. Moreover, a pronounced fluctuation in  $\langle G \rangle$  is observed when  $L > 10^5$ , attributed to the variations around the  $\langle G \rangle - E$  curve, particularly around the resonant peak at  $E \sim -1.027t$ . These results indicate that  $L = 10^3$  is the critical length for disordered BNRs to achieve stable resonant peaks across all the contact configurations. Since within this length, all the conductance contributed by non-resonant states decreases to nearly zero due to the successive scattering caused by random LDs, regardless of the contact configurations. The conductance contributed by resonant states remains unaffected by  $L$ , whereas the interface scattering between the disordered BNR and the  $\nu_{1/3}$  BNR or the SL electrode leads to a reduction in the resonant peaks.

Figures 4(d) and 4(f) show  $\langle G \rangle$  versus  $L$  at  $E \sim -1.027t$  and  $E \sim 0.249t$ , respectively, considering the contact configurations where the source electrode differs from the drain one. Several crucial characteristics can be summarized as follows. (i) The  $\nu_{1/5}$  BNR and  $\nu_{1/6}$  BNR electrodes do not affect the



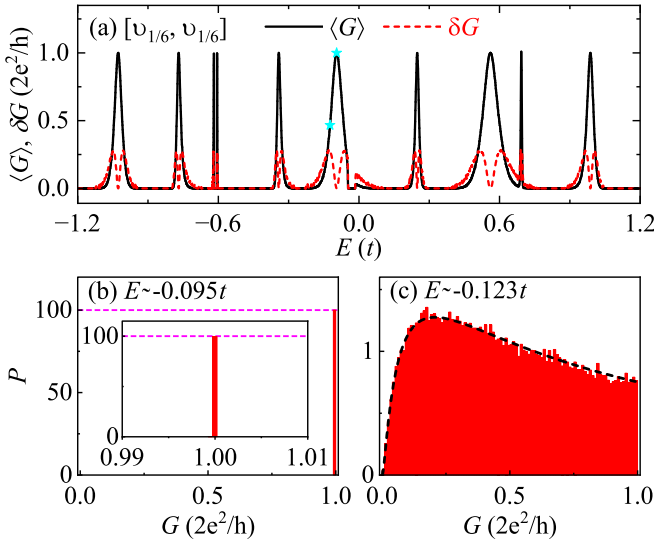


FIG. 5. Conductance fluctuations in disordered BNRs with contact configuration  $[v_{1/6}, v_{1/6}]$ . (a) Averaged conductance  $\langle G \rangle$  and standard deviation  $\delta G$  for disordered BNRs. (b) and (c) show the conductance distribution  $P(G)$  at  $E \sim -0.095t$  and  $-0.123t$ , indicated by the cyan stars in (a), respectively. The inset of (b) shows the same data of  $P(G)$  from (b) in a restricted range of conductance. The black-dashed line in (c) is the fitting curve obtained from Eq. (24), with  $s = 0.981$ . Here,  $N = 29$ .

amplitude of the resonant peaks at  $E \sim -1.027t$  and  $0.249t$  when  $L > 10^3$  [see the black-solid line in Figs. 4(d) and 4(f)]. In contrast, the  $v_{1/3}$  and SL electrodes will lead to the decrease of resonant peaks. (ii) If one of the electrodes is the  $v_{1/5}$  BNR, the  $\langle G \rangle$  at  $E \sim -1.027t$  is independent of  $L$  [see the black-solid, red-dashed, and blue-dotted lines in Fig. 4(d)]. (iii) If one of the electrodes is the  $v_{1/3}$  BNR, the conductance at  $E \sim 0.249t$  drops to 0 when  $L > 10^3$  [see the red-dashed, cyan-dashed-dotted, and orange-dashed-dotted lines in Fig. 4(f)]. (iv) When considering the SL electrode,  $\langle G \rangle$  at  $E \sim -1.027t$  displays more pronounced fluctuations as the value of  $L$  exceeds  $10^5$  [see blue-dotted, violet-dashed-dotted, and orange-dashed-dotted lines in Fig. 4(d)]. Consequently, the length-dependent electron transport in disordered BNRs is strongly dependent on the contact configurations. The amplitude of resonant peaks can be adjusted by modifying the source and drain electrodes when  $L > 10^3$ , allowing the creation of a stable conductance smaller than  $G_0$ .

### C. Conductance fluctuations and localization in disordered BNRs

To further understand the role of the contact effects and random LDs on the electron transport along disordered BNRs, we examine the conductance fluctuations. Figure 5(a) shows the energy-dependent averaged conductance  $\langle G \rangle$  and the standard deviation  $\delta G$  for disordered BNRs with  $N = 29$  under the contact configurations  $[v_{1/6}, v_{1/6}]$ . Here,  $\delta G \equiv \sqrt{\langle G^2 \rangle - \langle G \rangle^2}$ . It is noteworthy that the standard deviation at every resonant peak satisfies  $\delta G \sim 0$ , indicating that the resonant tunneling can occur in any disordered BNR with arbitrary arrangements of LDs [see the red-dashed line in

Fig. 5(a)]. As  $E$  deviates from the resonant energy,  $\delta G$  gradually increases. When the electron energy is further away from the resonant energy,  $\delta G$  decreases until it ultimately reaches zero. Moreover, it is evident that  $\delta G$  is exactly zero within the energy range of a small transmission gap in the resonant peak at  $E \sim -0.095t$ , indicating that the contact effects induced by the  $v_{1/6}$  BNR electrode is consistent across various disordered samples.

To further characterize the conductance fluctuations of these systems, we calculate the distributions of conductance  $P(G)$ . Here, we take the resonant peak at  $E \sim -0.095t$  as an example, and the result is applicable to any resonant peak. We focus on two specific energies:  $E \sim -0.095t$ , representing the energy of the resonant peak, and  $E \sim -0.123t$ , corresponding to the energy of maximal  $\delta G$ . For the reliability of the results,  $P(G)$  is determined through a statistical analysis of  $10^5$  disordered samples. It is clear that  $P(G_0) = 100\%$  when  $E \sim -0.095t$ , signifying that all the samples exhibit an identical conductance of  $G = G_0$  in this energy. This result remains valid even when a restricted range of conductance is considered, thereby confirming the robustness of the resonant tunneling [see the inset of Fig. 5(b)]. When the energy gradually deviates from the resonant energy, the conductance distribution widens, and  $\delta G$  gradually increases. When  $E \sim -0.123t$ ,  $\delta G$  reaches its maximum value, and its conductance distribution is shown in Fig. 5(c). It is clear that the conductance of all the disordered samples is distributed within the range  $[0, G_0]$ , indicating the presence of only one channel in this system when  $E \sim -0.123t$ . Within a scaling theory of Anderson localization, it is shown that the  $P(G)$  can be fitted by the following expression without free fitting parameters:

$$P_s(G) = C \frac{[\text{acosh}(1/\sqrt{G})]^{1/2}}{G^{3/2}(1-G)^{1/4}} e^{-(1/s)\text{acosh}^2(1/\sqrt{G})}, \quad (24)$$

which is used to study the conductance distribution of the disordered zigzag graphene nanoribbon near the Fermi energy [97]. Here,  $C$  is a normalization constant, and  $s = L/\lambda$  with  $\lambda$  the mean free path. The value of  $s$  can be determined numerically through the relation  $-\langle \ln G \rangle = L/\lambda$  [98]. As depicted in Fig. 5(c), the conductance distribution around the resonant energy of  $E \sim -0.123t$  is precisely described by Eq. (24), suggesting that the off-resonant states undergo standard Anderson localization due to the structural disorder induced by random LDs.

As a comparison, Fig. 6(a) displays the energy-dependent averaged conductance  $\langle G \rangle$  and standard deviation  $\delta G$  for the disordered BNR with  $N = 29$  in the contact configuration  $[v_{1/5}, v_{1/3}]$ . It is evident that despite the decrease in the amplitude of the resonant peaks due to the presence of the  $v_{1/3}$  BNR electrode, the condition  $\delta G \sim 0$  holds for every resonant peak. This implies that the conductance of resonant peaks consistently remains at a specific value smaller than  $G_0$  in every disordered sample. Given that their amplitude also remains independent of the size of the disordered BNRs, we can conclude that these resonant peaks with amplitude less than  $G_0$ , result from the interface scattering between the CSR and  $v_{1/3}$  electrode. Therefore disordered BNRs can be employed to attain a fixed conductance less than  $G_0$ , akin to

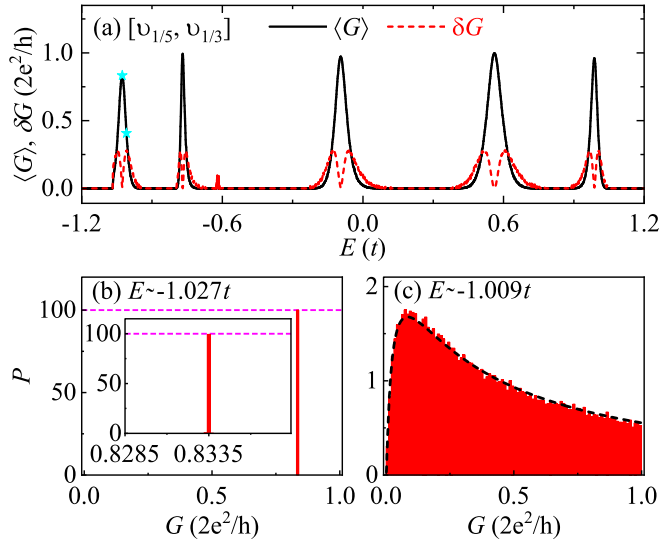


FIG. 6. Conductance fluctuations in disordered BNRs with contact configurations  $[\nu_{1/5}, \nu_{1/3}]$ . (a) Averaged conductance  $\langle G \rangle$  and standard deviation  $\delta G$  for disordered BNRs. (b) and (c) show the conductance distribution  $P(G)$  at  $E \sim -1.027t$  and  $-1.009t$ , indicated by the cyan stars in (a), respectively. The inset of (b) shows the same data of  $P(G)$  from (b) in a restricted range of conductance. The black-dashed line in (c) is the fitting curve obtained from Eq. (24), with  $s = 1.236$ . Here,  $N = 29$ .

the “0.7-anomaly” observed in quantum point contacts due to the many-body effects [99–101]. Moreover,  $\delta G$  is exactly zero when  $G$  disappears due to the contact effects of the  $\nu_{1/5}$  and  $\nu_{1/3}$  BNR electrodes. As a result, the contact effects of various electrodes on the electron transport along disordered BNRs remain consistent across different disordered samples.

Then, we compute  $P(G)$  at  $E \sim -1.027t$  and  $E \sim -1.009t$ . The former corresponds to the energy of the resonant peak with amplitude of  $G \sim 0.834G_0$ , while the latter corresponds to the energy of the maximum  $\delta G$  within the resonant peak. Figure 6(b) shows the conductance distribution  $P(G)$  at  $E \sim -1.027t$ . Remarkably, it is evident that  $P(0.834G_0) = 100\%$ , signifying that all the disordered samples share identical amplitude of resonant peaks at  $G \sim 0.834G_0$ , even within a restricted range of conductance [see the inset of Fig. 6(b)]. When  $E \sim -1.009t$ , the conductance is redistributed between the range of  $[0, G_0]$  and can be well fitted using the expression Eq. (24) [see Fig. 6(c)]. These results suggest that for certain disordered samples, the conductance at off-resonant energies can be greater than that at the resonant energies, which contradicts expectations based on the contact configuration  $[\nu_{1/6}, \nu_{1/6}]$ . This is attributed to the energy-dependent interface scattering strength between the CSR and the  $\nu_{1/3}$  BNR electrode. For electrons with resonant energies, the strength of the interface scattering they experience is fixed and independent of the disordered sample. While for electrons with off-resonant energies, the strength of the interface scattering varies with changes in the disordered sample, which may lead to a larger conductance.

#### D. Physical origin of different resonant peaks induced by $\nu_{1/3}$ electrode

As previously mentioned, the resonant peaks in the disordered BNRs with the  $\nu_{1/3}$  electrode can be classified into three categories based on the extent of suppression. Here, we explored the physical origin of the different resonant peaks induced by the  $\nu_{1/3}$  electrode. To illustrate this, we present the spatial distributions of bond currents for disordered BNRs in the contact configuration  $[\nu_{1/6}, \nu_{1/6}]$ , according to Eq. (8). Here, the results are shown for a specific disordered sample, and our findings hold for arbitrary disordered samples. Figures 7(a)–7(c) illustrate the spatial distributions of bond currents at the resonant energies  $E \sim -0.095t$ ,  $-0.342t$ , and  $-1.027t$  in the contact configuration  $[\nu_{1/6}, \nu_{1/6}]$ , corresponding to weakly suppressed, entirely suppressed, and strongly suppressed resonant peaks due to the contact effects of the  $\nu_{1/3}$  electrode, respectively. For any resonant energy, the spatial distributions within both the (2, 2) and (2, 3) chains remain unchanged as  $L$  increases, allowing electrons to propagate through the disordered BNR without experiencing dissipation, highlighting the nature of the resonant tunneling. However, at different resonant energies, the bond current distributions exhibit noticeable variations due to their distinct electron-transport modes. These differences in distribution are crucial in yielding varied suppression in different resonant peaks by the  $\nu_{1/3}$  BNR electrode.

For  $E \sim -0.095t$ , there is a continuous flow of current along the outer edges of each (2, 2) chain and along the armchair edges inside each (2, 3) chain [see Fig. 7(a)]. Specifically, there is almost no current passing through the hexagonal central atoms of the (2, 3) chain, allowing us to neglect these central atoms and treat the (2, 3) chain as the unit cell of the  $\nu_{1/3}$  BNR. Even though the tight-binding parameters are distinct, this electron-transport mode is potentially present in the  $\nu_{1/3}$  BNR electrode at the same resonant energy. Hence, if the  $\nu_{1/3}$  BNR electrode shares the same electron-transport mode at  $E \sim -0.095t$ , electrons will not encounter any interface scattering, and the resonant peaks at  $E \sim -0.095t$  will be well preserved in the contact configuration of the  $\nu_{1/3}$  BNR electrode. For  $E \sim -0.342t$ , the current flowing in the (2, 3) chain primarily passes through the central atoms and propagates along the horizontal direction, with almost no current distribution along the hexagonal edges [see Fig. 7(b)]. Furthermore, the vortex currents manifest at the upper and lower triangles of the central atoms in the (2, 3) chain, with their magnitude comparable to the inter-chain current. However, this electron-transport mode cannot match with any of the electron-transport modes in the  $\nu_{1/3}$  BNR electrode. Therefore the resonant peak at  $E \sim -0.342t$  is completely suppressed in the contact configuration of the  $\nu_{1/3}$  BNR electrode. The situation at  $E \sim -1.027t$  falls somewhere between the two just mentioned. As depicted in Fig. 7(c), the current flows along the outer edges of each (2, 2) chain, resembling the situation at  $E \sim -0.095t$ , while inside each (2, 3) chain, it follows in a zigzag path. Although the zigzag path involves both the edges and the central atoms of the (2, 3) chain, the current predominantly enters the (2, 3) chains through the hexagonal edges, which is also allowed for the electron-transport modes in the  $\nu_{1/3}$  BNR electrode.

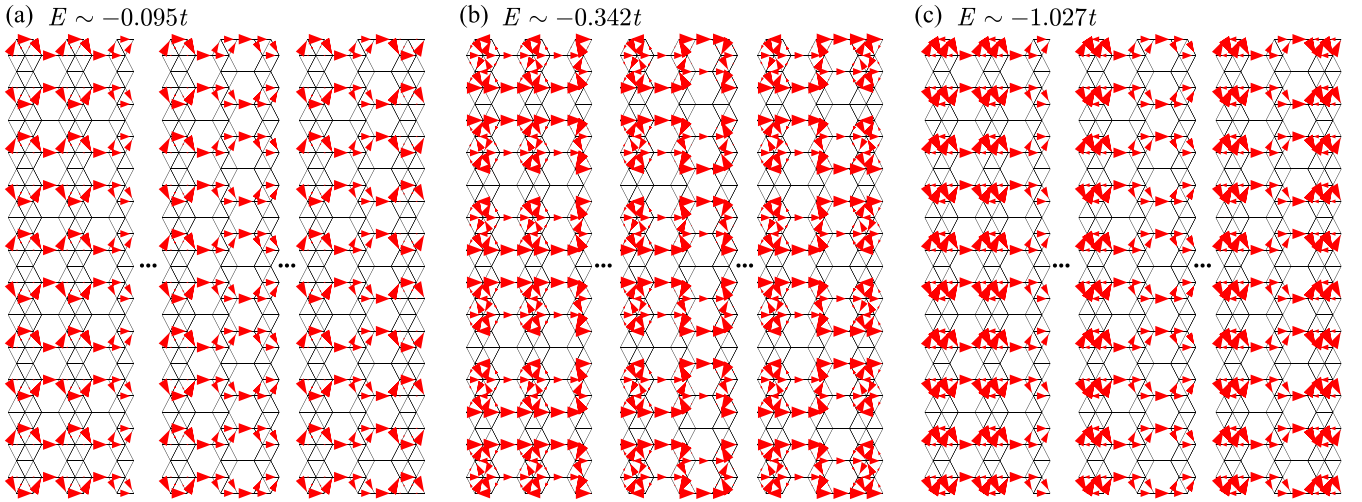


FIG. 7. The spatial distributions of bond currents at the resonant energies, (a)  $E \sim -0.095t$ , (b)  $\sim -0.342t$ , and (c)  $\sim -1.027t$ , are illustrated for a disordered BNR in the contact configuration  $[\nu_{1/6}, \nu_{1/6}]$ . These correspond to weakly suppressed, entirely suppressed, and strongly suppressed resonant peaks, respectively, due to the contact effect of the  $\nu_{1/3}$  electrode. The bond currents are indicated by red arrows, with the size proportional to their magnitude. Here,  $N = 29$  and  $L = 4000$ . For clarity, only partial chains is displayed.

However, the involvement of central atoms in this process causes mode mismatch, leading to the interface scattering and consequently a decrease in the amplitude of the resonant peaks. Consequently, the distinct resonant peaks induced by the  $\nu_{1/3}$  electrode can be comprehended through the analysis of the structure-property relationships associated with the local current distribution of the  $\nu_{1/3}$  and  $\nu_{1/6}$  BNRs. In fact, the weakly suppressed, entirely suppressed, and strongly suppressed can be attributed to the parallel, orthogonal, and overlapping wave functions between the electron states in the  $\nu_{1/3}$  BNR electrode and the resonant states in the disordered BNRs.

In addition, the distributions of bond current exhibit a clear periodicity along the width direction. For  $E \sim -0.095t$  and  $E \sim -1.027t$ , the current distribution in the disordered BNR with  $N = 29$  can be divided into 10 basic BNRs with a width of  $N_i = 2$  and a period of 3 [see Figs. 7(a) and 7(c)]. For  $E \sim -0.342t$ , the current distribution can be divided into 6 basic BNRs with a width of  $N_i = 4$  and a period of 5 [see Fig. 7(b)]. This can be linked to the earlier finding in Fig. 3, where identical resonant peaks can be found among the disordered BNRs with  $N = 29$  and  $N = 2$  as well as  $N = 4$ . The fact is that the bond current distributions for the resonant peaks at  $E \sim -0.095t$  and  $-1.027t$  in disordered BNRs with  $N = 2$  match with those in the basic BNRs with  $N_i = 2$ . Similarly, the bond current distributions for the resonant peak at  $E \sim -0.342t$  in disordered BNRs with  $N = 4$  coincide with those in the basic BNRs with  $N_i = 4$  (data not shown). Crucially, these results signify the evolution of resonant peaks in disordered BNRs with varying widths  $N$ , as further elaborated in Figs. 8 and 9.

### E. Two evolution phenomena for the resonant peaks in disordered BNRs with different width

We then focus on the evolution of resonant peaks in disordered BNRs with various  $N$ . Figure 8(a) shows  $\langle G \rangle$  vs  $E$

for disordered BNRs with  $N = 29, 14$ , and  $15$  for the contact configuration  $[\nu_{1/6}, \nu_{1/6}]$ . It clearly appears that some resonant peaks for  $N = 29$  perfectly superimpose on all those for  $N = 14$  [see the black-solid and red-dotted lines in Fig. 8(a)], including the resonant peak at  $E \sim -0.095t$ , suggesting that resonant peaks at the same energy in disordered BNRs with different  $N$  suffer from the same contact effects. More interestingly, the remaining resonant peaks for  $N = 29$  overlap well with all those for  $N = 15$  by appropriately adjusting peak positions [see the black-solid and blue-dashed lines in Fig. 8(a)]. Here arises the question: will the resonant peaks for  $N = 15$  and their corresponding ones in  $N = 29$

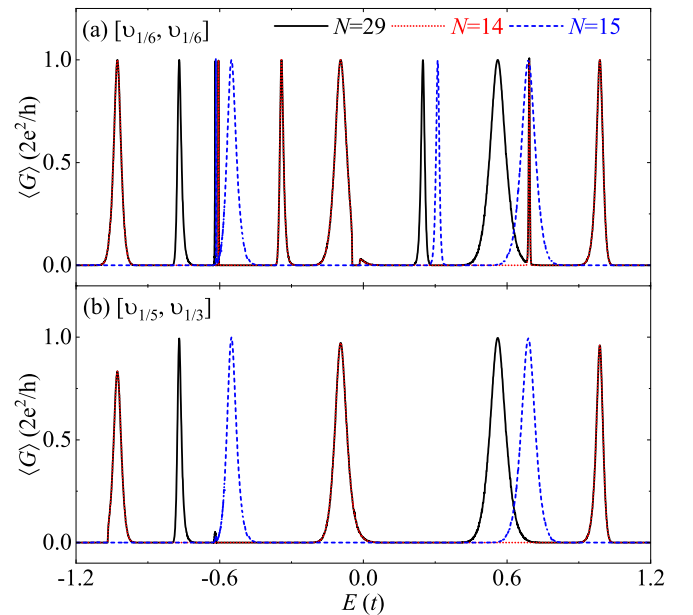


FIG. 8. Electron transport along disordered BNRs with widths  $N = 29, 14$ , and  $15$  for contact configurations (a)  $[\nu_{1/6}, \nu_{1/6}]$  and (b)  $[\nu_{1/5}, \nu_{1/3}]$ , respectively.

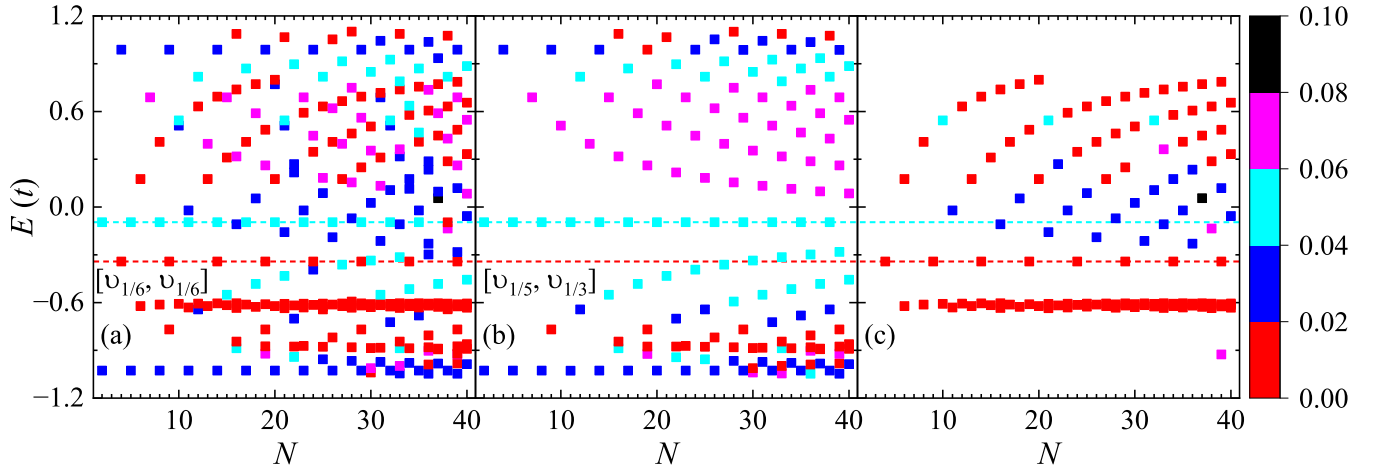


FIG. 9. A 2D plot of FWHM for all of the peaks vs  $N$  and  $E$  by considering the contact configurations (a)  $[\nu_{1/6}, \nu_{1/6}]$  and (b)  $[\nu_{1/5}, \nu_{1/3}]$ . (c) Evolution of disappearing peaks in the contact configuration  $[\nu_{1/5}, \nu_{1/3}]$  as compared to the  $[\nu_{1/6}, \nu_{1/6}]$ . The cyan and red lines display the evolution route of two resonant peaks initially appearing in disordered BNRs with width  $N_i = 2$  and  $4$ , respectively.

experience the same contact effects, even though their energies are different? However, no direct evidence could be provided in the contact configuration  $[\nu_{1/6}, \nu_{1/6}]$ .

Figure 8(b) shows  $\langle G \rangle$  versus  $E$  for the disordered BNRs with  $N = 29, 14$ , and  $15$  by considering the contact configuration  $[\nu_{1/3}, \nu_{1/5}]$ . Similarly, it is also evident that some resonant peaks for  $N = 29$  perfectly superimpose on all those for  $N = 14$  [see the black-solid and red-dotted lines in Fig. 8(b)], while the remaining ones overlap well with all those for  $N = 15$  by appropriately adjusting peak positions. As previously mentioned, the resonant peaks at  $E \sim 0.693t, 0.249t, -0.342t, -0.605t$  for  $N = 29$  are completely suppressed in the contact configuration  $[\nu_{1/3}, \nu_{1/5}]$ , owing to the contact effects of the  $\nu_{1/3}$  BNR electrode [see the black-solid lines in Figs. 8(a) and 8(b)]. The resonant peaks at identical energies,  $E \sim 0.693t, -0.342t$ , and  $-0.605t$  in the disordered BNR with  $N = 14$  are entirely suppressed, consistent with expectations. Notably, the resonant peak at  $0.311t$  for  $N = 15$ , corresponding to the one at  $0.249t$  for  $N = 29$ , is also completely suppressed [see the blue-dashed line in Fig. 8(b)]. This suggests that the contact effects on the resonant peaks is consistent between  $N = 15$  and  $N = 29$ , despite the change in peak position. The above phenomenon is widely observed in other disordered BNRs with odd widths  $N = N_o$ . Therefore we conclude that all of the resonant peaks of disordered BNRs with odd width  $N_o$  could be assembled from the ones with  $N = (N_o - 1)/2$  and  $N = (N_o + 1)/2$ , namely, evolution phenomenon (EP) I. The EP I is present in disordered BNRs, irrespective of the contact configurations. The contact effect is consistent for the resonant peaks in  $N = (N_o - 1)/2$  and  $N = (N_o + 1)/2$  with their respective counterparts in  $N = N_o$ .

Based on the above discussion, it is known that the disordered BNR with  $N = 29$  possesses identical resonant peaks as those observed in the disordered BNRs with  $N = 2, 4$ , and  $14$ . To further elucidate this phenomenon, Figs. 9(a) and 9(b) display a 2D plot of FWHM for all of the peaks as functions of  $N$  and  $E$  for the contact configurations  $[\nu_{1/6}, \nu_{1/6}]$  and  $[\nu_{1/5}, \nu_{1/3}]$ , respectively. In Fig. 9(b), only the resonant

peaks with amplitude larger than  $0.5G_0$  are taken into account for clarity. It is evident that numerous red points appear in the vicinity of  $E = -0.6t$  for the contact configuration  $[\nu_{1/6}, \nu_{1/6}]$ , indicating the widespread presence of the line-type resonant peaks [see Fig. 9(a)]. Due to the resonant peak filtering effect and the interface scattering of the  $\nu_{1/3}$  BNR electrode, the number of resonant peaks in Fig. 9(b) is significantly decreased as compared to those in Fig. 9(a). However, it is evident that the number of resonant peaks increases with the width  $N$  for both contact configurations, aligning with the previous discussion. Moreover, the FWHM of all the resonant peaks ranges from nearly 0 to  $0.1t$ , which provides an ideal standard for identifying different resonant peaks in the disordered BNRs with different  $N$ . By tracing resonant peaks with the same energy and FWHM in disordered BNRs with different values of  $N$ , an interesting EP can be identified.

For the contact configuration  $[\nu_{1/6}, \nu_{1/6}]$ , identical resonant peaks are observed at  $E \sim -0.095t$  for  $N = 2, 5, 8, \dots$  and at  $E \sim -0.342t$  for  $N = 4, 9, 14, \dots$  [see the cyan and red dashed lines in Fig. 9(a)]. While for the contact configuration  $[\nu_{1/5}, \nu_{1/3}]$ , similar phenomenon can also be detected that identical resonant peaks exist at  $E \sim -0.095t$  for  $N = 2, 5, 8, \dots$  [see the cyan-dashed line in Fig. 9(b)]. Therefore we conclude that a resonant peak that first emerges in the disordered BNR with  $N = N_i$  will reappear at the same energy  $E$  in various BNRs with  $N = \alpha(N_i + 1) - 1$ , where  $\alpha$  is an integer and  $N_i + 1$  is the period. This characteristic is referred as EP II, which compensates for EP I. Because of the resonant peak filtering effect induced by the  $\nu_{1/3}$  BNR, some resonant peaks will completely vanish for the contact configuration  $[\nu_{1/5}, \nu_{1/3}]$ , as discussed above. Figure 9(c) shows the evolution of disappearing peaks by subtracting the points in Fig. 9(b) from those in Fig. 9(a). One can see that the disappearing peaks usually possess small FWHM [see the red and blue squares in Fig. 9(c)], indicating that the resonant peaks with small FWHM is more sensitive to external factors like the electrode. Additionally, the disappearing resonant peaks occur at  $E \sim -0.342t$  for  $N = 4, 9, 14, \dots$  [see the red-dashed line

in Fig. 9(c)], which is the same as EP II. This implies that a resonant peak that first disappears in the disordered BNR with  $N = N_i$ , induced by the resonant peak filtering effect, will always disappear at the same energy in various BNRs with  $N = \alpha(N_i + 1) - 1$ . Note that  $29 = 10 \times (2 + 1) - 1 = 6 \times (4 + 1) - 1$ , the disordered BNR with  $N = 29$  includes all the resonant peaks of  $N = 2$  and  $N = 4$ . As the resonant peak at  $E \sim -0.342t$  in the disordered BNR with  $N = 4$  is completely suppressed by the  $\nu_{1/3}$  BNR, the resonant peak at the same energy also disappears in the disordered BNR with  $N = 29$ .

The EP II can be understood by considering a disordered BNR with  $N = \alpha(N_i + 1) - 1$ , which can be divided into  $\alpha$  basic BNRs with width  $N_i$ . Here, the  $m$ th basic BNR includes the rows from  $n = m_i - N_i$  to  $m_i - 1$ , and is separated from the  $(m + 1)$ th one by the  $m_i$ th row, with  $0 < m < \alpha$  and  $m_i = m(N_i + 1)$ . For instance, the BNR with  $N = 29$  can be divided into 6 basic BNRs with  $N_i = 4$ , which are separated by the 5th, 10th, 15th, 20th, and 25th rows [see Fig. 7(b)]. Then, the Hamiltonian  $\mathbf{H}_c$  of disordered BNR with width  $N$  can then be rewritten as:

$$\mathbf{H}_c = \begin{bmatrix} \mathbf{H}_1 & \mathbf{A}_{11} & 0 & \cdots & 0 \\ \mathbf{A}_{11}^\dagger & \mathbf{R}_1 & \mathbf{A}_{21} & \ddots & \vdots \\ 0 & \mathbf{A}_{21}^\dagger & \mathbf{H}_2 & \ddots & 0 \\ \vdots & \ddots & \ddots & \ddots & \mathbf{A}_{\alpha,\alpha-1} \\ 0 & \cdots & 0 & \mathbf{A}_{\alpha,\alpha-1}^\dagger & \mathbf{H}_\alpha \end{bmatrix}, \quad (25)$$

where  $\mathbf{H}_m$  and  $\mathbf{R}_m$  are the sub-Hamiltonians of the  $m$ th basic BNR and the  $m_i$ th row, respectively, and  $\mathbf{A}_{mn}$  the hopping matrix from the  $m_i$ th row to the  $m$ th basic BNR when  $n = m$  and from the  $m$ th BNR to the  $m_i - 1$ th row when  $n = m - 1$ . Since the  $m$ th and  $m + 1$ th BNRs are mirror images about the  $m_i$ th row, the eigenstates of  $\mathbf{H}_m$  and  $\mathbf{H}_{m+1}$  are the same with identical eigenenergies, and the hopping matrices satisfy  $\mathbf{A}_{m+1,m} = \mathbf{A}_{m,m}^\dagger$ . Assuming the resonant state of the  $m$ th basic BNR is described by the Schrödinger equation of

$$\mathbf{H}_m |\Phi_0\rangle = E_r |\Phi_0\rangle, \quad (26)$$

with  $|\Phi_0\rangle$  the wave function and  $E_r$  the resonant energy. Accordingly, the wave function  $|\Psi\rangle$  of  $\mathbf{H}_c$  can then be constructed as:

$$|\Psi\rangle = \sqrt{\alpha} / \alpha (|\Phi_0\rangle, 0, -|\Phi_0\rangle, \dots, (-1)^{\alpha-1} |\Phi_0\rangle)^\top \quad (27)$$

and the resonant state of disordered BNR with width  $N$  can be described by Schrödinger equation:

$$\mathbf{H}_c |\Psi\rangle = E_r |\Psi\rangle. \quad (28)$$

As a result, the disordered BNR with width  $N = \alpha(N_i + 1) - 1$  share the identical resonant peaks with the basic disordered BNR with width  $N_i$ . During the simulation of electron transport in nanoribbons, the main source of computational complexity arises from the width of the nanoribbons. As the width of the nanoribbon increases, higher computational costs

are incurred. However, these two EPs allow us to deduce the resonant peaks of wide disordered BNR from the narrow one without the need for practical calculation.

#### IV. CONCLUSION

In conclusion, we study theoretically the contact effects on the electron transport through two-terminal disordered BNRs by considering inhomogeneous tight-binding parameters. We demonstrate that, although the overall electron transport ability is significantly affected by randomly distributed LDs, several resonant peaks appear in the transmission spectra, irrespective of inhomogeneous parameters, nanoribbon length and width, and contact configurations. The profile and amplitude of resonant peaks can be modified by considering various contact configurations. Specifically, in the contact configurations  $[\nu_{1/5}, \nu_{1/5}]$  or  $[\nu_{1/6}, \nu_{1/6}]$ , the profile of certain specific resonant peaks changes due to the absence of electron-transport modes in the electrodes, while the amplitude of all the resonant peaks remains at  $G_0$ . In the contact configuration  $[\nu_{1/3}, \nu_{1/3}]$  or  $[\text{SL}, \text{SL}]$ , the amplitude of all the resonant peaks decreases to values below  $G_0$ . Particularly, the resonant peaks under the contact configuration  $[\nu_{1/3}, \nu_{1/3}]$  can be categorized into three types: weakly suppressed, strongly suppressed, and completely suppressed. This categorization indicates the presence of the resonant peak filtering effect, elucidated through the analysis of the local bond current distributions. Furthermore, we find that distinct contact effects accumulate when considering different source and drain electrodes. Besides, we show that the number of resonant peaks increases with  $N$ , and resonant peaks in disordered BNRs with varying  $N$  may undergo a similar contact effect. By tracking all the resonant peaks in disordered BNRs with different  $N$ , we can confirm the existence of two evolution phenomena. This study systematically explores the electron transport through disordered BNRs with LDs under various contact configurations, offering an effective method for tuning the electron transport properties in disordered BNRs. Overall, our results can help to understand the structure-property relationships and hold significant application prospects in the fabrication of electronic devices based on BNRs. Finally, we point out that we only consider the electron transport across the rows of hollow hexagons, and different phenomena will be observed for electron propagation along the rows of hollow hexagons because of the anisotropy of the borophene, which may deserve further investigation.

#### ACKNOWLEDGMENTS

This work is supported by the National Natural Science Foundation of China (Grants No. 12274466, No. 11874428, No. 12374034, and No. 11921005), the Innovation Program for Quantum Science and Technology (2021ZD0302403), the Strategic priority Research Program of Chinese Academy of Sciences (Grant No. XDB28000000), the Hunan Provincial Science Fund for Distinguished Young Scholars (Grant No. 2023JJ10058), and the High Performance Computing Center of Central South University.

- [1] K. S. Novoselov, A. K. Geim, S. V. Morozov, D. Jiang, Y. Zhang, S. V. Dubonos, I. V. Grigorieva, and A. A. Firsov, Electric field effect in atomically thin carbon films, *Science* **306**, 666 (2004).
- [2] A. H. Castro Neto, F. Guinea, N. M. R. Peres, K. S. Novoselov, and A. K. Geim, The electronic properties of graphene, *Rev. Mod. Phys.* **81**, 109 (2009).
- [3] S. Das Sarma, Shaffique Adam, E. H. Hwang, and E. Rossi, Electronic transport in two-dimensional graphene, *Rev. Mod. Phys.* **83**, 407 (2011).
- [4] S. Wang, P. K. Ang, Z. Wang, A. L. L. Tang, J. T. L. Thong, and K. P. Loh, High mobility, printable, and solution-processed graphene electronics, *Nano Lett.* **10**, 92 (2010).
- [5] P. Avouris, Graphene: Electronic and photonic properties and devices, *Nano Lett.* **10**, 4285 (2010).
- [6] Y.-W. Son, M. L. Cohen, and S. G. Louie, Half-metallic graphene nanoribbons, *Nature (London)* **444**, 347 (2006).
- [7] V. Barone, O. Hod, and G. E. Scuseria, Electronic structure and stability of semiconducting graphene nanoribbons, *Nano Lett.* **6**, 2748 (2006).
- [8] L. Yang, C.-H. Park, Y.-W. Son, M. L. Cohen, and S. G. Louie, Energy band-gap engineering of graphene nanoribbons, *Phys. Rev. Lett.* **99**, 186801 (2007).
- [9] P. Vogt, P. D. Padova, C. Quaresima, J. Avila, E. Frantzeskakis, M. C. Asensio, A. Resta, B. Ealet, and G. L. Lay, Silicene: Compelling experimental evidence for graphenelike two-dimensional silicon, *Phys. Rev. Lett.* **108**, 155501 (2012).
- [10] L. Chen, C. C. Liu, B. J. Feng, X. Y. He, P. Cheng, Z. J. Ding, S. Meng, Y. G. Yao, and K. H. Wu, Evidence for Dirac fermions in a honeycomb lattice based on silicon, *Phys. Rev. Lett.* **109**, 056804 (2012).
- [11] M. E. Dávila, L. Xian, S. Cahangirov, A. Rubio, G. L. Lay, Germanene: A novel two-dimensional germanium allotrope akin to graphene and silicene, *New J. Phys.* **16**, 095002 (2014).
- [12] L. F. Li, S. Z. Lu, J. Pan, Z. Qin, Y. Q. Wang, Y. Q. Wang, Y. L. Wang, G. Y. Cao, S. X. Du, and H. J. Gao, Buckled germanene formation on Pt(111), *Adv. Mater.* **26**, 4820 (2014).
- [13] L. K. Li, Y. J. Yu, G. J. Ye, Q. Q. Ge, X. D. Ou, H. Wu, D. L. Feng, X. H. Chen, and Y. B. Zhang, Black phosphorus field-effect transistors, *Nat. Nanotechnol.* **9**, 372 (2014).
- [14] A. J. Mannix, X.-F. Zhou, B. Kiraly, J. D. Wood, D. Alducin, B. D. Myers, X. Liu, B. L. Fisher, U. Santiago, J. R. Guest, M. J. Yacaman, A. Ponce, A. R. Oganov, M. C. Hersam, and N. P. Guisinger, Synthesis of borophenes: Anisotropic, two-dimensional boron polymorphs, *Science* **350**, 1513 (2015).
- [15] B. Feng, J. Zhang, Q. Zhong, W. Li, S. Li, H. Li, P. Cheng, S. Meng, L. Chen, and K. Wu, Experimental realization of two-dimensional boron sheets, *Nat. Chem.* **8**, 563 (2016).
- [16] R. M. Westervelt, Graphene nanoelectronics, *Science* **320**, 324 (2008).
- [17] D. Akinwande, N. Petrone, and J. Hone, Two-dimensional flexible nanoelectronics, *Nat. Commun.* **5**, 5678 (2014).
- [18] T. Radsar, H. Khalesi, and V. Ghods, Graphene properties and applications in nanoelectronic, *Opt. Quantum Electron.* **53**, 178 (2021).
- [19] X. Xu, T. Guo, M. Lanza, and H. N. Alshareef, Status and prospects of MXene-based nanoelectronic devices, *Matter* **6**, 800 (2023).
- [20] F. Schwierz, Graphene transistors, *Nat. Nanotechnol.* **5**, 487 (2010).
- [21] Y. Yu, Illarionov, T. Knobloch, M. Jech, M. Lanza, D. Akinwande, M. I. Vexler, T. Mueller, M. C. Lemme, G. Fiori, F. Schwierz, and T. Grasser, Insulators for 2D nanoelectronics: The gap to bridge, *Nat. Commun.* **11**, 3385 (2020).
- [22] R. Qing, M. Xue, J. Zhao, L. Wu, A. Breitwieser, E. Smorodina, T. Schubert, G. Azzellino, D. Jin, J. Kong, T. Palacios, U. B. Sleytr, and S. Zhang, Scalable biomimetic sensing system with membrane receptor dual-monolayer probe and graphene transistor arrays, *Sci. Adv.* **9**, eadf1402 (2023).
- [23] X. Liu and M. C. Hersam, 2D materials for quantum information science, *Nat. Rev. Mater.* **4**, 669 (2019).
- [24] Z. Cheng, R. Cao, K. Wei, Y. Yao, X. Liu, J. Kang, J. Dong, Z. Shi, H. Zhang, and X. Zhang, 2D materials enabled next-generation integrated optoelectronics: From fabrication to applications, *Adv. Sci.* **8**, 2003834 (2021).
- [25] K. Kanahashi, J. Pu, and T. Takenobu, 2D materials for large-area flexible thermoelectric devices, *Adv. Energy Mater.* **10**, 1902842 (2020).
- [26] H. Tang and S. Ismail-Beigi, Novel precursors for boron nanotubes: The competition of two-center and three-center bonding in boron sheets, *Phys. Rev. Lett.* **99**, 115501 (2007).
- [27] K. C. Lau and R. Pandey, Stability and electronic properties of atomistically-engineered 2D boron sheets, *J. Phys. Chem. C* **111**, 2906 (2007).
- [28] X. Yang, Y. Ding, and J. Ni, Ab initio prediction of stable boron sheets and boron nanotubes: Structure, stability, and electronic properties, *Phys. Rev. B* **77**, 041402(R) (2008).
- [29] H. Tang and S. Ismail-Beigi, Self-doping in boron sheets from first principles: a route to structural design of metal boride nanostructures, *Phys. Rev. B* **80**, 134113 (2009).
- [30] H. Tang and S. Ismail-Beigi, First-principles study of boron sheets and nanotubes, *Phys. Rev. B* **82**, 115412 (2010).
- [31] E. S. Penev, S. Bhowmick, A. Sadrzadeh, and B. I. Yakobson, Polymorphism of two-dimensional boron, *Nano Lett.* **12**, 2441 (2012).
- [32] X. Wu, J. Dai, Y. Zhao, Z. Zhuo, J. Yang, and X. C. Zeng, Two-dimensional boron monolayer sheets, *ACS Nano* **6**, 7443 (2012).
- [33] W.-L. Li, X. Chen, T. Jian, T.-T. Chen, J. Li, and L.-S. Wang, From planar boron clusters to borophenes and metalloborophenes, *Nat. Rev. Chem.* **1**, 0071 (2017).
- [34] Z. Zhang, Y. Yang, G. Gao, and B. I. Yakobson, Two-dimensional boron monolayers mediated by metal substrates, *Angew. Chem. Int. Ed.* **54**, 13022 (2015).
- [35] Z. Zhang, E. S. Penev, and B. I. Yakobson, Two-dimensional boron: Structures, properties and applications, *Chem. Soc. Rev.* **46**, 6746 (2017).
- [36] P. Ranjan, T. K. Sahu, R. Bhushan, S. S. Yamijala, D. J. Late, P. Kumar, and A. Vinu, Borophene: Freestanding borophene and its hybrids, *Adv. Mater.* **31**, 1970196 (2019).
- [37] B. Feng, J. Zhang, R.-Y. Liu, T. Iimori, C. Lian, H. Li, L. Chen, K. Wu, S. Meng, F. Komori, and I. Matsuda, Direct evidence of metallic bands in a monolayer boron sheet, *Phys. Rev. B* **94**, 041408(R) (2016).
- [38] Q. Zhong, J. Zhang, P. Cheng, B. Feng, W. Li, S. Sheng, H. Li, S. Meng, L. Chen, and K. Wu, Metastable phases of 2D boron sheets on Ag (111), *J. Phys.: Condens. Matter* **29**, 095002 (2017).

- [39] W. Li, L. Kong, C. Chen, J. Gou, S. Sheng, W. Zhang, H. Li, L. Chen, P. Cheng, and K. Wu, Experimental realization of honeycomb borophene, *Sci. Bull.* **63**, 282 (2018).
- [40] R. Wu, I. K. Drozdov, S. Eltinge, P. Zahl, S. Ismail-Beigi, I. Božović, and A. Gozar, Large-area single-crystal sheets of borophene on Cu (111) surfaces, *Nat. Nanotechnol.* **14**, 44 (2019).
- [41] B. Kiraly, X. Liu, L. Wang, Z. Zhang, A. J. Mannix, B. L. Fisher, B. I. Yakobson, M. C. Hersam, and N. P. Guisinger, Borophene synthesis on Au (111), *ACS Nano* **13**, 3816 (2019).
- [42] N. A. Vinogradov, A. Lyalin, T. Taketsugu, A. S. Vinogradov, and A. Preobrajenski, Single-phase borophene on Ir (111): Formation, structure, and decoupling from the support, *ACS Nano* **13**, 14511 (2019).
- [43] R. Wu, S. Eltinge, I. K. Drozdov, A. Gozar, P. Zahl, J. T. Sadowski, S. Ismail-Beigi, and I. Božović, Micrometrescale single-crystalline borophene on a square-lattice Cu (100) surface, *Nat. Chem.* **14**, 377 (2022).
- [44] A. J. Mannix, Z. Zhang, N. P. Guisinger, B. I. Yakobson, and M. C. Hersam, Borophene as a prototype for synthetic 2D materials development, *Nat. Nanotechnol.* **13**, 444 (2018).
- [45] Q. Zhong, L. Kong, J. Gou, W. Li, S. Sheng, S. Yang, P. Cheng, H. Li, K. Wu, and L. Chen, Synthesis of borophene nanoribbons on Ag(110) surface, *Phys. Rev. Mater.* **1**, 021001(R) (2017).
- [46] Q. Li, L. Wang, H. Li, M. K. Y. Chan, and M. C. Hersam, Synthesis of quantum-confined borophene nanoribbons, *ACS Nano* **18**, 483 (2024).
- [47] B. Feng, O. Sugino, R.-Y. Liu, J. Zhang, R. Yukawa, M. Kawamura, T. Iimori, H. Kim, Y. Hasegawa, H. Li, L. Chen, K. Wu, H. Kumigashira, F. Komori, T.-C. Chiang, S. Meng, and I. Matsuda, Dirac fermions in borophene, *Phys. Rev. Lett.* **118**, 096401 (2017).
- [48] M. Ezawa, Triplet fermions and Dirac fermions in borophene, *Phys. Rev. B* **96**, 035425 (2017).
- [49] S. Gupta, A. Kutana, and B. I. Yakobson, Dirac cones and nodal line in borophene, *J. Phys. Chem. Lett.* **9**, 2757 (2018).
- [50] B. Feng, J. Zhang, S. Ito, M. Arita, C. Cheng, L. Chen, K. Wu, F. Komori, O. Sugino, K. Miyamoto, T. Okuda, S. Meng, and I. Matsuda, Discovery of 2D anisotropic Dirac cones, *Adv. Mater.* **30**, 1704025 (2018).
- [51] E. S. Penev, A. Kutana, and B. I. Yakobson, Can two-dimensional boron superconduct? *Nano Lett.* **16**, 2522 (2016).
- [52] M. Gao, Q. Z. Li, X. Z. Yan, and J. Wang, Prediction of phonon-mediated superconductivity in borophene, *Phys. Rev. B* **95**, 024505 (2017).
- [53] Y. Zhao, S. Zeng, C. Lian, Z. Dai, S. Meng, and J. Ni, Multigap anisotropic superconductivity in borophenes, *Phys. Rev. B* **98**, 134514 (2018).
- [54] F. Norouzi, M. Farokhnezhad, M. Esmailzadeh, and B. Szafran, Controllable spin filtering and half-metallicity in  $\beta_{12}$ -borophene nanoribbons, *Phys. Rev. B* **104**, 245431 (2021).
- [55] Y. Kang, K. Yang, J. Fu, Z. Wang, X. Li, Z. Lu, J. Zhang, H. Li, J. Zhang, and W. Ma, Selective interfacial excited-state carrier dynamics and efficient charge separation in borophene-based heterostructures, *Adv. Mater.* **36**, 2307591 (2024).
- [56] X. Liu, Z. Zhang, L. Wang, B. I. Yakobson, and M. C. Hersam, Intermixing and periodic self-assembly of borophene line defects, *Nat. Mater.* **17**, 783 (2018).
- [57] L. Kong, L. Liu, L. Chen, Q. Zhong, P. Cheng, H. Li, Z. Zhang, and K. Wu, One-dimensional nearly free electron states in borophene, *Nanoscale* **11**, 15605 (2019).
- [58] Y. Wang, L. Kong, C. Chen, P. Cheng, B. Feng, K. Wu, and L. Chen, Realization of regular-mixed quasi-1D borophene chains with long-range order, *Adv. Mater.* **32**, 2005128 (2020).
- [59] X. Liu, L. Wang, S. Li, M. S. Rahn, B. I. Yakobson, and M. C. Hersam, Geometric imaging of borophene polymorphs with functionalized probes, *Nat. Commun.* **10**, 1642 (2019).
- [60] L. Liu, Z. Zhang, X. Liu, X. Xuan, B. I. Yakobson, M. C. Hersam, and W. Guo, Borophene concentric superlattices via self-assembly of twin boundaries, *Nano Lett.* **20**, 1315 (2020).
- [61] Q. Li, V. S. C. Kolluru, M. S. Rahn, E. Schwenker, S. Li, R. G. Hennig, P. Darancet, M. K. Chan, and M. C. Hersam, Synthesis of borophane polymorphs through hydrogenation of borophene, *Science* **371**, 1143 (2021).
- [62] X. Liu, L. Wang, B. I. Yakobson, and M. C. Hersam, Nanoscale probing of image-potential states and electron transfer doping in borophene polymorphs, *Nano Lett.* **21**, 1169 (2021).
- [63] S.-G. Xu, C.-C. He, Y.-J. Zhao, H. Xu, and X.-B. Yang, Unconventional line defects engineering in two-dimensional boron monolayers, *Phys. Rev. Mater.* **5**, 044003 (2021).
- [64] P.-J. Hu, S.-X. Wang, X.-F. Chen, Z.-R. Liang, T.-F. Fang, A.-M. Guo, H. Xu, and Q.-F. Sun, Resonant tunneling in disordered borophene nanoribbons with line defects, *npj Comput. Mater.* **8**, 131 (2022).
- [65] P.-J. Hu, J.-T. Ding, Z.-R. Liang, T.-F. Fang, A.-M. Guo, and Q.-F. Sun, Enhanced electron transport and self-similarity in quasiperiodic borophene nanoribbons with line defects, *Nanoscale* **15**, 10740 (2023).
- [66] J. Liang, Y. Wang, Z. Yang, L.-C. Xu, L. Xue, R. Liu and X. Liu, A theoretical study on the line defects in  $\beta_{12}$ -borophene: Enhanced direct-current and alternating-current conductances, *Phys. Chem. Chem. Phys.* **25**, 6067 (2023).
- [67] K. S. Novoselov, A. Mishchenko, A. Carvalho, and A. H. Castro Neto, 2D materials and van der Waals heterostructures, *Science* **353**, 461 (2016).
- [68] G. Iannaccone, F. Bonaccorso, L. Colombo, and G. Fiori, Quantum engineering of transistors based on 2D materials heterostructures, *Nat. Nanotechnol.* **13**, 183 (2018).
- [69] M. Gibertini, M. Koperski, A. F. Morpurgo, and K. S. Novoselov, Magnetic 2D materials and heterostructures, *Nat. Nanotechnol.* **14**, 408 (2019).
- [70] P. V. Pham, S. C. Bodepudi, K. Shehzad, Y. Liu, Y. Xu, B. Yu, and X. Duan, 2D heterostructures for ubiquitous electronics and optoelectronics: Principles, opportunities, and challenges, *Chem. Rev.* **122**, 6514 (2022).
- [71] X. Liu, Z. Wei, I. Balla, A. J. Mannix, N. P. Guisinger, E. Luijten, and M. C. Hersam, Self-assembly of electronically abrupt borophene/organic lateral heterostructures, *Sci. Adv.* **3**, e1602356 (2017).
- [72] X. Liu and M. C. Hersam, Borophene-graphene heterostructures, *Sci. Adv.* **5**, eaax6444 (2019).
- [73] L. Li, J. F. Schultz, S. Mahapatra, X. Liu, C. Shaw, X. Zhang, M. C. Hersam, and N. Jiang, Angstrom-scale spectroscopic visualization of interfacial interactions in an organic/borophene vertical heterostructure, *J. Am. Chem. Soc.* **143**, 15624 (2021).

- [74] R. Liu, C. Hou, X. Liang, Z. Wu, and G. Tai, Borophene-ZnO heterostructures: Preparation and application as broadband photonic nonvolatile memory, *Nano Res.* **16**, 5826 (2023).
- [75] D. S. Schulman, A. J. Arnold, and S. Das, Contact engineering for 2D materials and devices, *Chem. Soc. Rev.* **47**, 3037 (2018).
- [76] Y. M. Blanter and I. Martin, Transport through normal-metal-graphene contacts, *Phys. Rev. B* **76**, 155433 (2007).
- [77] J. P. Robinson and H. Schomerus, Electronic transport in normal-conductor/graphene/normal-conductor junctions and conditions for insulating behavior at a finite electron-carrier density, *Phys. Rev. B* **76**, 115430 (2007).
- [78] E. J. H. Lee, K. Balasubramanian, R. T. Weitz, M. Burghard, and K. Kern, Contact and edge effects in graphene devices, *Nat. Nanotechnol.* **3**, 486 (2008).
- [79] G. Liang, N. Neophytou, M. S. Lundstrom, and D. E. Nikonov, Contact effects in graphene nanoribbon transistors, *Nano Lett.* **8**, 1819 (2008).
- [80] G. Giovannetti, P. A. Khomyakov, G. Brocks, V. M. Karpan, J. van den Brink, and P. J. Kelly, Doping graphene with metal contacts, *Phys. Rev. Lett.* **101**, 026803 (2008).
- [81] S. Barraza-Lopez, M. Vanevic, M. Kindermann, and M. Y. Chou, Effects of metallic contacts on electron transport through graphene, *Phys. Rev. Lett.* **104**, 076807 (2010).
- [82] A. Pieper, G. Schubert, G. Wellein, and H. Fehske, Effects of disorder and contacts on transport through graphene nanoribbons, *Phys. Rev. B* **88**, 195409 (2013).
- [83] T. Stegmann, J. A. Franco-Villafane, U. Kuhl, F. Mortessagne, and T. H. Seligman, Transport gap engineering by contact geometry in graphene nanoribbons: Experimental and theoretical studies on artificial material, *Phys. Rev. B* **95**, 035413 (2017).
- [84] P. Lv, N. Dai, and Q.-F. Sun, Double refraction and spin splitter in normal-conductor/hexagonal-semiconductor junctions, *Phys. Rev. B* **97**, 235425 (2018).
- [85] J. A. Vergés, G. Chiappe, E. San-Fabián, and E. Louis, Conductance through the armchair graphene nanoribbons 9-AGNR: Strong dependence on contact to leads, *Phys. Rev. B* **98**, 155415 (2018).
- [86] K. Čerņevičs, O. V. Yazyev, and M. Pizzochero, Electronic transport across quantum dots in graphene nanoribbons: Toward built-in gap-tunable metal-semiconductor-metal heterojunctions, *Phys. Rev. B* **102**, 201406(R) (2020).
- [87] N. Moreau, B. Brun, S. Somanchi, K. Watanabe, T. Taniguchi, C. Stampfer, and B. Hackens, Contacts and upstream modes explain the electron-hole asymmetry in the graphene quantum Hall regime, *Phys. Rev. B* **104**, L201406 (2021).
- [88] Y. Wang, J. C. Kim, Y. Li, K. Y. Ma, S. Hong, M. Kim, H. S. Shin, H. Y. Jeong, and M. Chhowalla, P-type electrical contacts for 2D transition-metal dichalcogenides, *Nature (London)* **610**, 61 (2022).
- [89] H. Schomerus, Effective contact model for transport through weakly-doped graphene, *Phys. Rev. B* **76**, 045433 (2007).
- [90] E. Gomes and F. Moraes, Current vortices in hexagonal graphene quantum dots, *Phys. Rev. B* **104**, 165408 (2021).
- [91] M. L. Sancho, J. L. Sancho, and J. Rubio, Quick iterative scheme for the calculation of transfer matrices: Application to Mo (100), *J. Phys. F: Met. Phys.* **14**, 1205 (1984).
- [92] M. L. Sancho, J. L. Sancho, J. L. Sancho, and J. Rubio, Highly convergent schemes for the calculation of bulk and surface green functions, *J. Phys. F: Met. Phys.* **15**, 851 (1985).
- [93] C. H. Lewenkopf and E. R. Mucciolo, The recursive Green's function method for graphene, *J. Comput. Electron.* **12**, 203 (2013).
- [94] H. Haug and A. P. Jauho, *Quantum Kinetics in Transport and Optics of Semiconductors* (Springer, Berlin, 1996).
- [95] L. Sun and Y. Guo, Line-type resonance peaks and their suppression through graphene-based symmetric and asymmetric double barriers, *J. Appl. Phys.* **109**, 123719 (2011).
- [96] D. Liu, B. Liu, R. Yuan, J. Zheng, and Y. Guo, Valley filter and valley valve based on WSe<sub>2</sub> double-barrier junctions modulated by polarized light, *Phys. Rev. B* **103**, 245432 (2021).
- [97] I. Klefogiannis and I. Amanatidis, Conductance through disordered graphene nanoribbons: Standard and anomalous electron localization, *Phys. Rev. B* **88**, 205414 (2013).
- [98] V. A. Gopar and R. A. Molina, Controlling conductance statistics of quantum wires by driving ac fields, *Phys. Rev. B* **81**, 195415 (2010).
- [99] S. M. Cronenwett, H. J. Lynch, D. Goldhaber-Gordon, L. P. Kouwenhoven, C. M. Marcus, K. Hirose, N. S. Wingreen, and V. Umansky, Low-temperature fate of the 0.7 structure in a point contact: A kondo-like correlated state in an open system, *Phys. Rev. Lett.* **88**, 226805 (2002).
- [100] F. Bauer, J. Heyder, E. Schubert, D. Borowsky, D. Taubert, B. Bruognolo, D. Schuh, W. Wegscheider, J. v. Delft, and S. Ludwig, Microscopic origin of the '0.7-anomaly' in quantum point contacts, *Nature (London)* **501**, 73 (2013).
- [101] M. J. Iqbal, R. Levy, E. J. Koop, J. B. Dekker, J. P. de Jong, J. H. M. van der Velde, D. Reuter, A. D. Wieck, R. Aguado, Y. Meir, and C. H. van der Wal, Odd and even Kondo effects from emergent localization in quantum point contacts, *Nature (London)* **501**, 79 (2013).